FOUR-PRONG π^-p INTERACTIONS

AT 250 GeV/c

Ph.D. Thesis
by

James Scouras

May 1980

UNIVERSITY OF MARYLAND
DEPARTMENT OF PHYSICS AND ASTRONOMY
COLLEGE PARK, MARYLAND

Title of Dissertation: Four-Prong π^-p Interactions at

250 GeV/c

Name of Candidate: James Scouras

Doctor of Philosophy, 1980

Dissertation and Abstract Approved: _____

Chung Y. Chang

Associate Professor

Department of Physics and Astronomy

University of Maryland

Date Approved: _____

ABSTRACT

Title of Dissertation: Four-prong π^-p Interactions at

                                        250 GeV/c

James Scouras, Doctor of Philosophy, 1980

Dissertation directed by: Associate Professor Chung Y. Chang

                                        Department of Physics and Astronomy

                                        University of Maryland

Four-prong π^-p interactions from the Fermilab hydrogen-filled fifteen-foot bubble chamber exposed to a 250 GeV/c π^- beam are studied. The data sample consists of 1292 events. Phenomenological characteristics of the interaction (notably beam and target diffractive dissociation) are described using single particle inclusive distributions in transverse momentum squared, Feynman X, and rapidity for π^-, π^+, and protons. The results of a search for the production of resonances are presented. Lower bounds on the cross-sections for inclusive $\rho^0(770)$ and $\Delta^{++}(1232)$ production are .42 ± .09 mb and .49 ± .07 mb, respectively. The cross-section for the reaction $\pi^-p \rightarrow \pi^-\pi^+\pi^-p$ is 625 ± 80 μb. The cross-section for ρ^0 production in this channel is 149 ± 43 μb.

FOUR-PRONG π^-p INTERACTIONS

AT 250 GeV/c

by
James Scouras

Dissertation submitted to the Faculty of the Graduate School
of the University of Maryland in partial fulfillment
of the requirements for the degree of
Doctor of Philosophy
1980

Dedicated to my wife, Kathy,

whose love and support have sustained me

through these difficult years

TABLE OF CONTENTS

LIST OF TABLES

LIST OF FIGURES

CHAPTER I

INTRODUCTION

Although its future is somewhat in doubt,[1] the bubble chamber has long been one of the most useful particle detectors in high energy physics. The desirability of using a bubble chamber as soon as possible as the highest available energies led to the transfer in 1972 of the thirty-inch chamber from Argonne National Laboratory to Fermi National Accelerator Laboratory.[2] At the same time, the construction of a much larger, fifteen-foot, chamber was undertaken. This experiment was conducted in the fall of 1974 during the engineering run of the fifteen-foot chamber,[3] which had the combined purpose of testing the chamber's operating characteristics and providing data for the study of hadronic interactions at high energy. Approximately 41,000 pictures were taken of the hydrogen-filled chamber exposed to a π^- beam at 250 GeV/c.

There has been substantial effort devoted to the study of diffractive phenomena in hadronic collisions at high energies since the opening of the CERN Intersecting Storage Rings and Fermi National Accelerator Laboratory. It has been found that a significant fraction ($\sim$20%) of the final states of hadronic interactions can be described by the diffractive fragmentation (or dissociation) of the beam and/or the target.[2] In this model the interaction is a two-step process in which the beam (target) is excited to a higher energy state while the target (beam) is deflected intact (the leading particle). The excited state of the beam-like (target-like) particle subsequently fragments into ordinary hadrons such

as pions, kaons and low-mass resonant states. Beam and target diffrac-
tion processes for π^-p interactions are schematically represented in
Figure I-1.

Diffraction dissociation has been studied using distribution in the
masses of the systems recoiling from the leading particles. Substantial
peaks at low mass have provided evidence for the diffractive excitation
of the target or beam into states with masses up to 5-6 GeV.[4] Additional
evidence has come from distributions in Feynman X for identified reaction
products, where a peak near $X_F = \pm 1$ can be identified with the leading
particle.[5]

Another topic of substantial interest in the study of hadronic
physics is the observation of resonance production. Resonance
decay products account for a significant fraction of observed reaction
products. In addition they may contribute to an explanation of the
observed correlations between particles with small rapidity gaps.[6]

In this study we present an analysis of four-prong final states of
π^-p interactions at 250 GeV/c, concentrating on the diffractive nature of
the interaction and possible resonance production. Four-prong events are
selected for this study since the dominant contribution to diffractive
processes have been found in low multiplicity ($\leq$ 6 prongs) interactions.[4]
Furthermore the number of entries in effective mass distributions of
various combinations of reaction products is smaller than the number of
entries for higher multiplicity events. This provides the potential for
a higher signal to noise ratio in a search for resonances. An additional
advantage of four-prong events over higher multiplicity events is that
they have a greater probability of giving a constrained fit to a particular

Beam diffraction

π⁻ → decay products of excited π⁻

p → p → leading proton

Target diffraction

π⁻ → π⁻ → leading π⁻

p̄ → decay products of excited proton
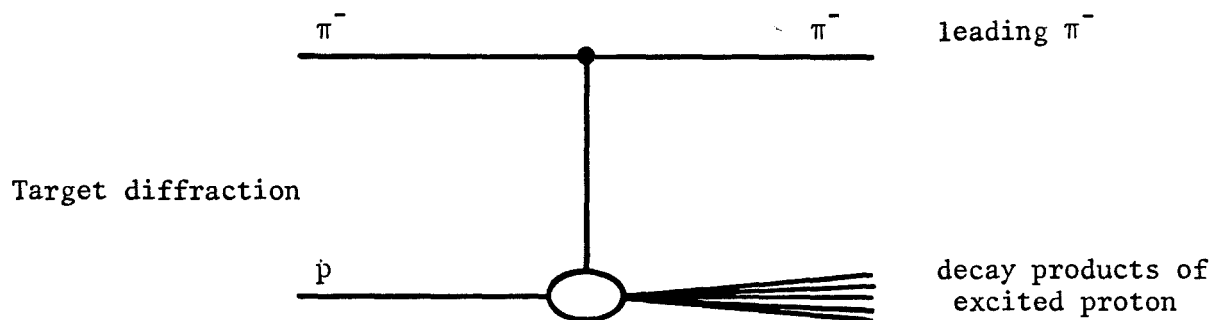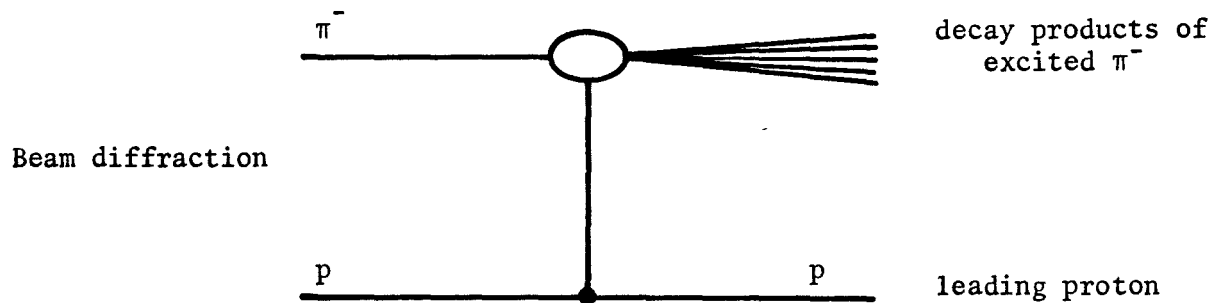
Figure I-1: Schematic representation of beam and target diffractive dissociation in π⁻p interactions.

reaction. Thus information on the exclusive reaction

$$\pi^- p \rightarrow \pi^- \pi^+ \pi^- p$$

can be obtained, including the cross-section, the diffractive nature of the reaction, and resonance production in this channel.

The fifteen-foot chamber is an excellent tool for these studies. The large volume and path length available enable a more precise momentum determination of secondaries. This is especially true for protons stopping within the chamber, for which the momentum can be determined from range information, rather than curvature.

Details of the data collection process are found in Chapter II. The analysis of the data through the preparation of the Data Summary Tape (DST) is described in Chapter III.

In Chapter IV some phenomenological characteristics of the interaction are examined by studying single-particle inclusive reactions. These are reactions of the form

$$\pi^- p \rightarrow a + X,$$

where "a" represents a specific observed particle and "X" represents the remainder of the final state, which may be partially unobserved. The advantage of studying inclusive reactions is that the analysis of the data and presentation of the results is straightforward. Of course, much information is lost by lumping the rest of the final state into the system "X". However, general features such as the leading particle effect and the diffractive nature of the interaction can be studied with this method. Distributions in transverse momentum squared, Feynman X, and rapidity for π^-, π^+, and protons are presented. Also the system "X" in the reaction

$$\pi^- p \rightarrow p + X$$

is examined for evidence of beam dissociation.

In Chapter V results of a search for the production of reso-nances[7] are presented, using the effective mass distributions of $(\pi^+\pi^-)$, $(\pi^+\pi^-\pi^\pm)$, $(p\pi^\pm)$, and $(p\pi^-\pi^\pm)$ combinations.

In Chapter VI the exclusive reaction
$$\pi^- p \to \pi^- \pi^+ \pi^- p$$
is examined. Estimates of the cross-sections for this reaction, as well as the ratio of the beam to target diffractive components, are made. Results of a resonance search are presented for all possible two- and three-particle effective mass distributions in this reaction.

CHAPTER I

References

1. One of the major problems is that the bubble chamber can make no

   selection on the type of interaction. As interactions of interest

   become more rare, more film must be processed to find these events.

   In addition, as incident energies increase, the complexity of the

   resultant events increases to such an extent that scanning and meas-

   uring the film becomes very time-consuming.

2. For a review of experimental results obtained from the thirty-inch

   chamber at Fermilab, see J. Whitmore, Physics Reports 10C, 274 (1974)

   and J. Whitmore, Physics Reports 27C, 187 (1976).

3. F.R. Huson, P. Berge, D. Bogert, R. Hanft, R. Harris, S. Kahn,

   J. Lannutti, and T. Murphy, Fermi National Accelerator Report No.

   FN-282 (1975).

4. F.C. Winkelmann, Phys. Letts. 48B, 273 (1974).

5. J. Whitmore et al, Phys. Rev. D16, 3137 (1977).

6. A.W. Chao and C. Quigg, Phys. Rev. D9, 2016 (1974).

7. For a list of known resonances in various stages of confirmation and

   their properties see Phys. Letts. 75B, No. 1 (1978).

CHAPTER II

DATA ACQUISITION

The source of the data analyzed in this study is a "bare" bubble

chamber experiment conducted in October, 1974 at Fermi National

Accelerator Laboratory by a collaboration of Florida State University

and Fermilab. Approximately 41,000 exposures of the fifteen-foot

hydrogen-filled bubble chamber were obtained with an incident π^- beam

momentum of 250 GeV/c.

The initial pass on the data emphasized analysis of multiplicity

distributions, neutral strange particle production, and gamma ray

production. Results of these studies have been previously reported.[1]

On the second pass measurements of a fraction of the two-, four-, and

six-prong events were made primarily to study the exclusive reactions:

$$\pi^- p \rightarrow \pi^- p$$

$$\pi^- p \rightarrow \pi^- \pi^+ \pi^- p$$

$$\pi^- p \rightarrow \pi^- \pi^+ \pi^- \pi^+ \pi^- p$$

These measurements were completed by Florida State University and

Fermilab in June, 1977.

In 1975 the collaboration was expanded to include the University

of Maryland, the University of California at Riverside, and the Univer-

sity of Notre Dame in a similar run at 360 GeV/c. In addition, in

early 1978 the University of Maryland obtained for analysis the raw

measurements of the aforementioned low-multiplicity events. This

study is restricted to an analysis of the four-prong events, which total
1292 and represent 42% of the entire observed sample.

A. The Beam

A schematic representation of the Fermilab accelerator, beam lines,
and target areas appears in Figure II-1. Protons for the main ring are
produced and accelerated to 750 keV by a Cockroft-Walton accelerator.
They are subsequently accelerated in turn by a linear accelerator (to
200 MeV), a booster synchrotron (to 8 GeV), and the main ring synchrotron
(to 300 GeV).

The fifteen-foot bubble chamber is located in the Neutrino Area,
a more detailed schematic of which is shown in Figure II-2. The primary
beam for the Neutrino Area consists of 300 GeV protons extracted from the
main ring and delivered to the upstream end of the Enclosure 99 (Neuhall)
into beam lines N0 and N7. The N0 line produces the neutrino beam for
the fifteen-foot bubble chamber and the muon beam (N1). The N7 line
produces the secondary hadron beam for both the thirty-inch and fifteen-
foot chambers.

The protons are steered by N7 to the production target in Enclosure
100. Immediately downstream from the target a pair of magnets selects
the desired production angle. The beam is then directed by line N3-N5
to Enclosure 101 which contains the momentum-selection magnets and a
pair of quadrupoles which focus the beam horizontally and vertically
at the momentum slit in Enclosure 103. The momentum bite is determined
using a horizontal collimator at the momentum slit. For this experiment
negatively charged particles produced at an angle of 1 milliradian with
a momentum of 250 GeV/c and a momentum bite of ± .1% comprise the selected
secondary beam.
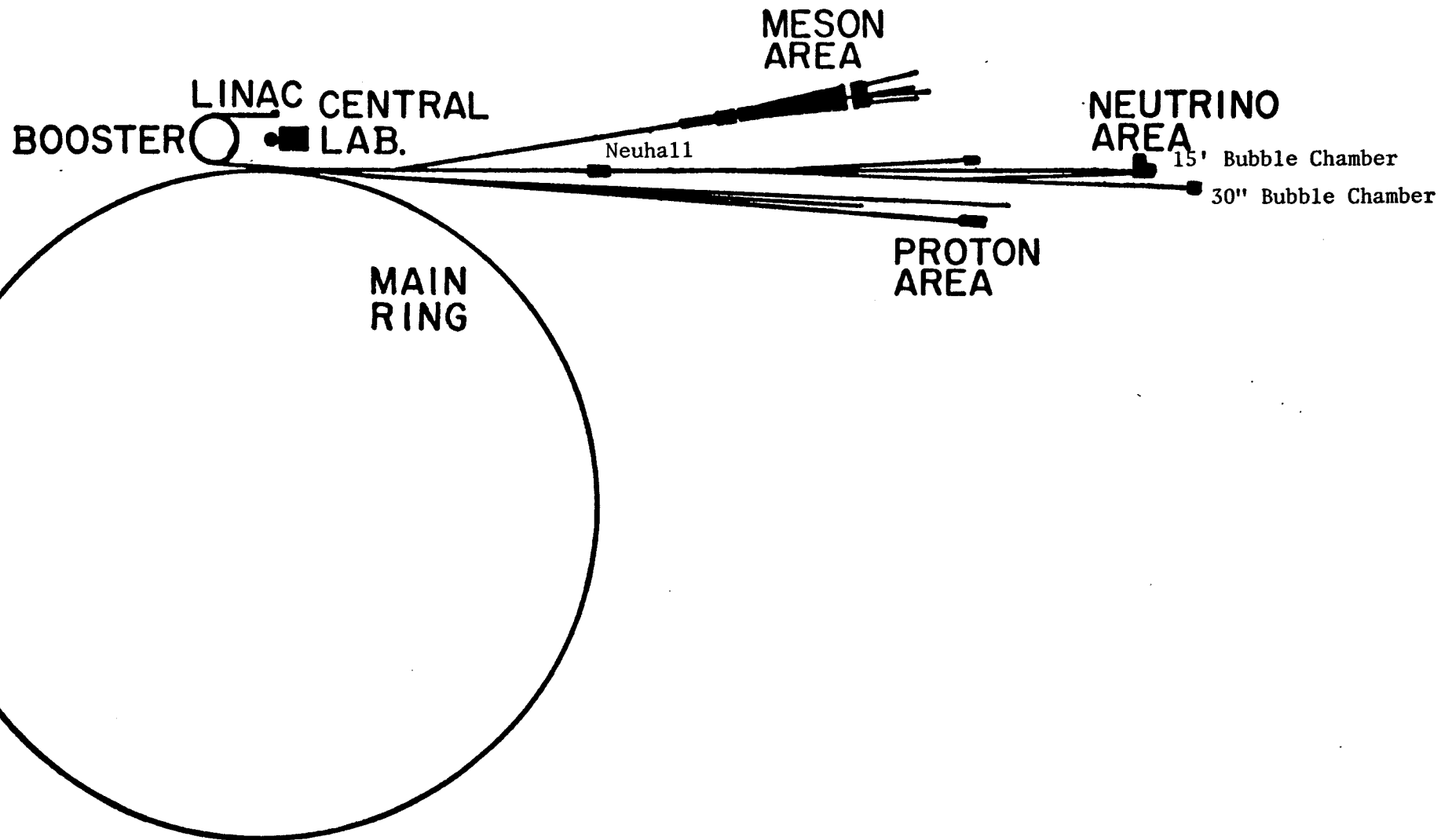
Figure II-1: Fermi National Accelerator Laboratory accelerators and target areas.
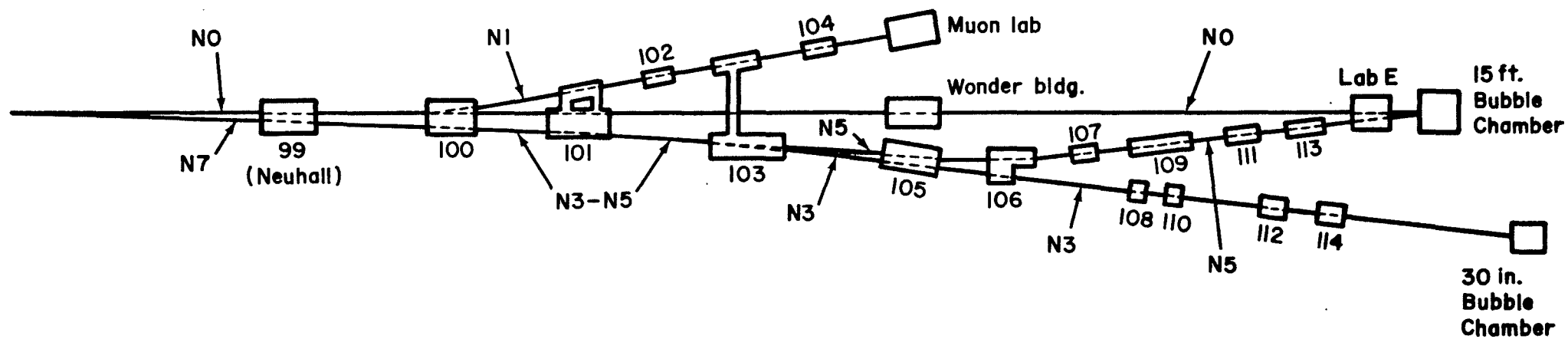
Figure II-2: Neutrino area beam lines.

The N3 and N5 lines are separated with a horizontal bend in Enclosure 103. The beam follows line N5 for the remainder of the distance to the fifteen-foot chamber. This line contains mainly bending and focusing magnets and makes no additional selection on beam momentum or composition.

The estimated composition of the beam at the chamber entrance appears in Table II-1. These values come from assuming the same contamination as reported for π^- at 205 GeV/c since that run similarly selected negative particles at a production angle of 1 milliradian with a $\pm$ .1% momentum bite[2]. The k^- and $\bar{p}$ contaminations were measured at 205 GeV/c using a Cerenkov counter, and the μ^- contamination was determined from upstream absorption measurements.

The beam profile (full width at half maximum), measured 200 cm. upstream from the center of the chamber, was 1.5 cm. in the vertical direction and 30 cm. in the horizontal direction. The angular divergence was 4 milliradians in the vertical plane and 8 milliradians in the horizontal plane.

A kicker magnet was employed to decrease the number of conjested frames by limiting the number of primary interactions that could occur on any single picture. This resulted in an average of approximately 4 beam tracks and .6 primary interactions per exposure.

TABLE II-1

ESTIMATED BEAM COMPOSITION[2]

Particle	Percent
π^-	95.84 ± .55
μ^-	2.6 ± .5
k^-	1.4 ± .2
$\bar{p}$	.16 ± .10

B. The Bubble Chamber

Top and side views of the Fermilab fifteen-foot bubble chamber appear in Figure II-3.[3] The chamber may be more accurately described as a twelve-foot (inside diameter) sphere, with the addition of a "nose" at the chamber entrance which increases the length along the beam direction to fifteen feet.

There are six cameras arranged in two sets of three each, so that the chamber may be used for both a neutrino and a hadron experiment at the same time. The hadron cameras comprise the triad positioned to look more deeply into the nose, since only the hadron beam is visible. Unfortunately, due to the rapidly varying magnetic field in the nose, track reconstruction using measured points in this region is unreliable. However, the nose still serves to more clearly distinguish true beam tracks and secondary prongs from upstream interactions.

The optics system includes fisheye lenses for a larger field of view (108°),70 mm. film, and Scotchlite reflecting tape on the inner walls of the chamber. The average demagnification on film is 60, which is relatively large and limits the observation of low energy protons.

Although the chamber's superconducting magnet is capable of producing a central field of 30 kilogauss using a current of 5000 Amperes, the data for this experiment were taken with a field of 21 kilogauss.

The special advantages of the fifteen-foot chamber relevant to the topic of this study are the large path length and volume available. This enables a more precise momentum determination of secondaries and easier particle identification. In particular, observing heavily

49

2.5°

NEUTRINO ₵

HADRON ₵

2.5°

<u>Top View</u>

108°

CHAMBER LIQUID
H₂,D₂, OR Ne

NEUTRINO & HADRON
BEAM DIRECTION

3"

<u>Side View</u>

EL.745'-3"

SCOTCHLITE

Figure II-3: Fifteen-
foot bubble chamber.

0   5 FT.
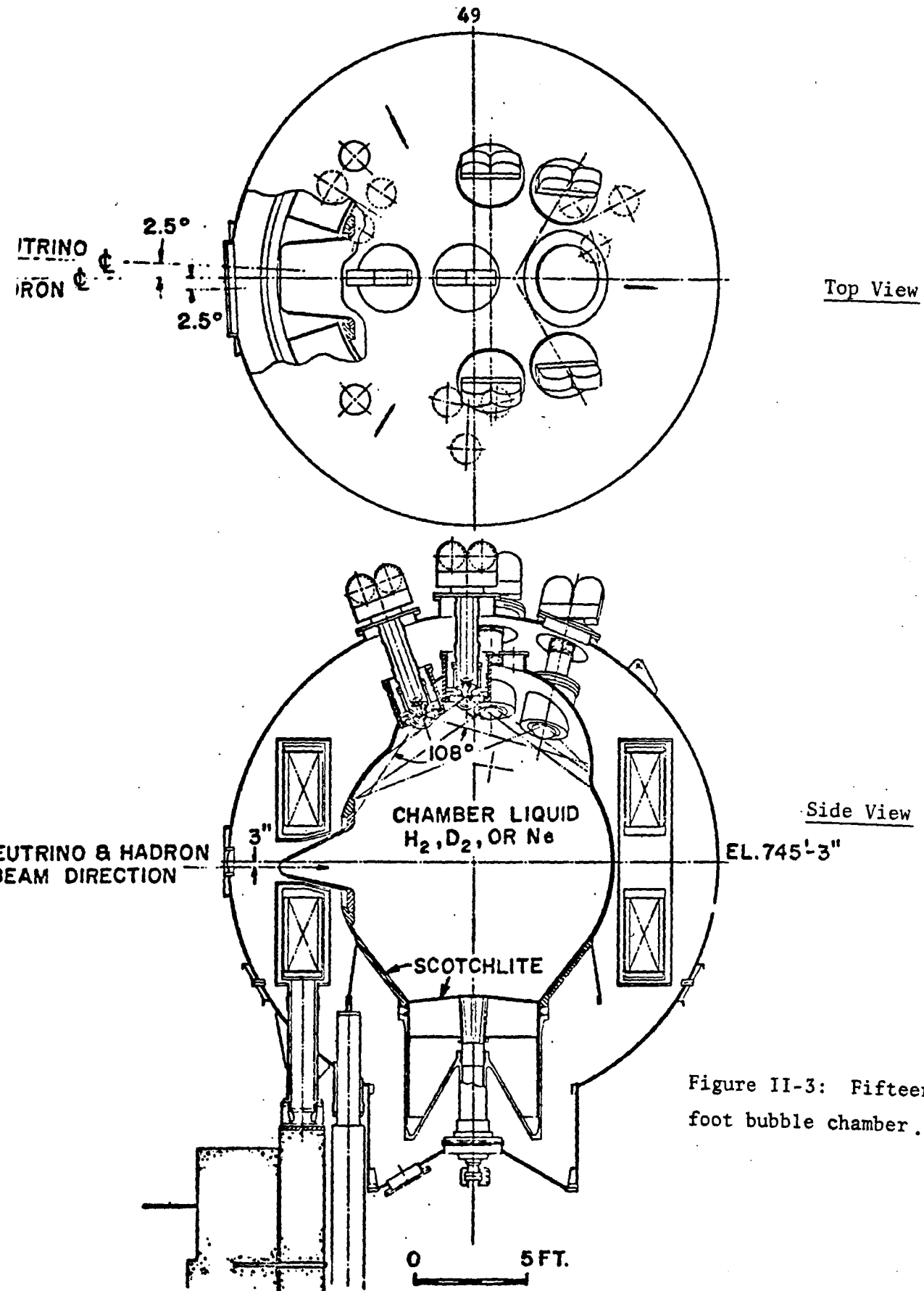
ionized positive stopping tracks provides a useful method for identify-

ing protons. Even with these advantages a substantial fraction (up to

$\sim$ 12%, depending on particle type) of the tracks have insufficient

curvature for an accurate ($\Delta p/p <$ .25) measurement of momentum. This

is primarily due to the combination of high beam momentum, low magnetic

field, and the low multiplicity of events (which yield a larger average

momentum per particle) selected for this study.

CHAPTER II

References

1. S. Hagopian, J.R. Albright, P. Hays, and J.E. Lannutti, Florida State Univ. Report No. FSU-HEP-76-1-02, 1976 (unpublished).

    P.J. Hays, R.N. Diamond, R.K. Clark, S. Hagopian, J.E. Lannutti, J.P. Berge, D. Bogert, R. Hanft, R. Harris, F.R. Huson, S. Kahn, and W. Smart, Florida State Univ. Report No. FSU-HEP-79-18-12, 1979 (submitted to Phys. Rev.).

    D. Bogert, R. Hanft, R. Harris, F.R. Huson, S. Kahn, C. Pascaud, W.M. Smart, J.R. Albright, S. Hagopian, P. Hays, and J.E. Lannutti, Phys. Rev. $\underline{D16}$, 2098 (1977).

    R. Harris, D. Bogert, R. Hanft, F.R. Huson, S. Kahn, W. Smart, N.N. Biswas, J.M. Bishop, N.M. Cason, V.P. Kenney, W.D. Shephard, J.R. Albright, S. Hagopian, P. Hays, and J.E. Lannutti, Phys. Rev. $\underline{D18}$, 92 (1978).

    Patrick J. Hays, Ph.D. thesis, Florida State University 1980, (unpublished).

2. D. Ljung, D. Bogert, R. Hanft, F.R. Huson, S. Kahn, C. Pascaud, S. Pruss, W.M. Smart, H.H. Bingham, D.M. Chew, B.Y. Daugeras, W.B. Fretter, G. Goldhaber, W.R. Graves, A.D. Johnson, J.A. Kadyk, L. Stutte, G.H. Trilling, F.C. Windelmann, and G.P. Yost, Phys. Rev. $\underline{D15}$, 3163 (1977).

3. For further detail on the status of the 15-foot bubble chamber near the time of this experiment see F.R. Huson, P. Berge, D. Bogert, R. Hanft, R. Harris, S. Kahn, J. Lannutti, and T. Murphy, Fermi National Accelerator Laboratory Report No. FN-282 (1975), from which this drawing was reproduced.

CHAPTER III

DATA PROCESSING

The data analysis procedure used for this study appears in schematic form in Figure III-1. The film was scanned and measured by Florida State University and Fermilab; all subsequent analysis was performed at the University of Maryland. There was already a geometry program, TVGP,[1] for the fifteen-foot chamber in existence at the University of Maryland at the time the raw measurements were received. The decision was made, therefore, to adapt this version to the measurements rather than to import the HYDRA[2] geometry program then in use at Fermilab.

First the measurement tape was rewritten to be readable with standard Fortran programs. It was then rewritten a second time to conform to TVGP input (BRAVE[3] output) format.

The next step in the chain of analysis depended on whether or not the event was track-matched. An event is track-matched if it is deliberately measured so that the first track measured in view 1 corresponds to the first track measured in view 2, etc. These events will hereinafter be referred to as Experiment 24, or matched, events. The events for which this matching was not deliberately done during the measurement process will hereinafter be referred to as Experiment 59, or unmatched events. MATCH[4] is the set of subroutines which can be incorporated within TVGP to track-match events. Unmatched events were processed by TVGP with MATCH; matched events were processed both by TVGP without MATCH and by TVGP with MATCH (as a check on both MATCH and the measurements).

Measurements for events which failed TVGP were plotted in an attempt to ascertain the cause of the failure. If it was decided that the event
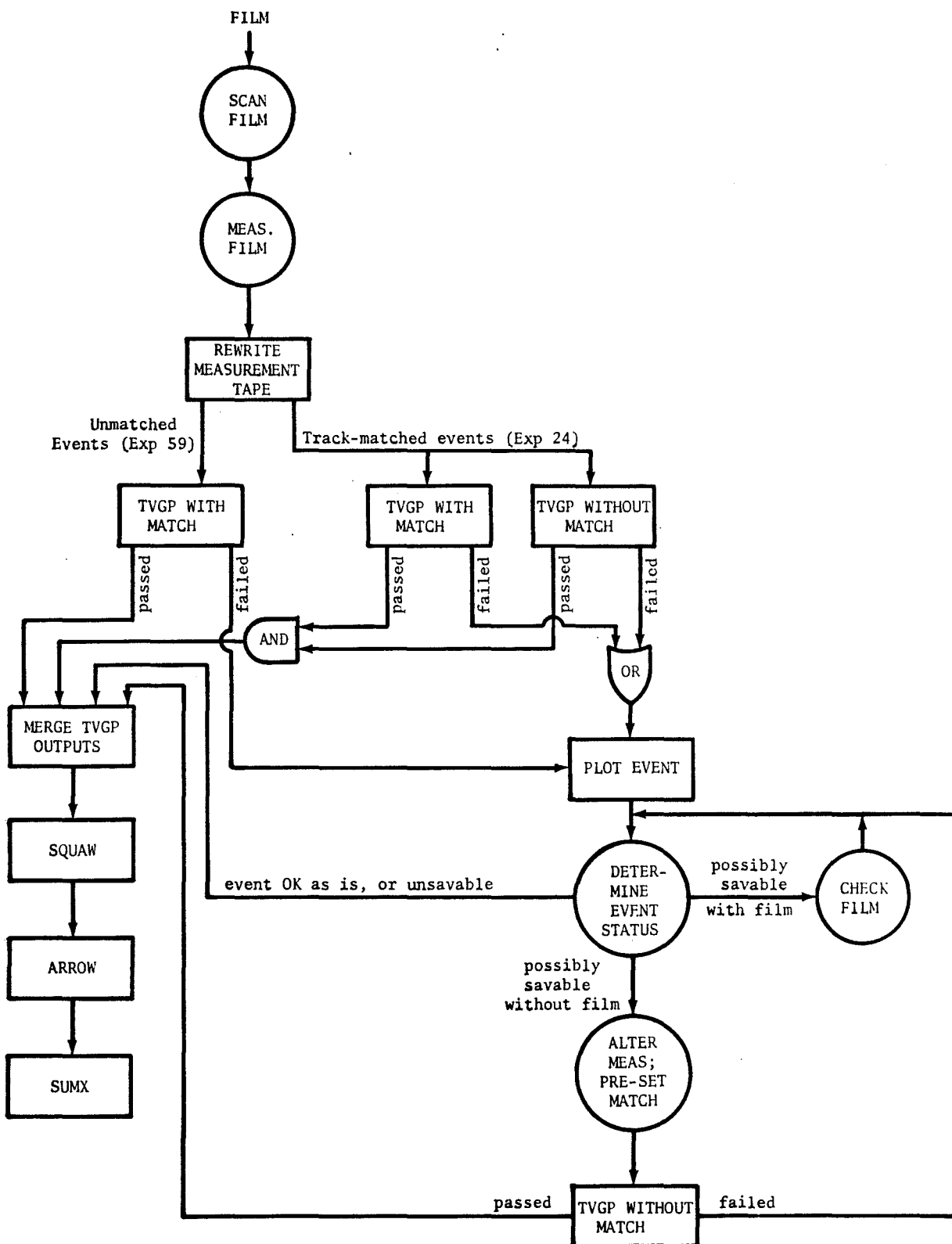
Figure III-1: The data analysis procedure. Circles represent steps with major human involvement; rectangles represent computer programs.

might be saved by altering the raw measurements or preselecting the correct match (with or without looking at the film), this was done and the event was re-processed by TVGP.

The final TVGP output tape consisted of events which passed the initial geometry program(s), events which failed the initial geometry program(s) but were later saved, and events which failed the initial geometry program(s) and were either deemed hopeless, or remained unsaved after one or more attempts. These events were then processed through SQUAW[5] (kinematic fitting), ARROW[6] (DST preparation), and finally by SUMX[7] (cuts on the data, physics calculations, particle identification, histograms, diplots, etc.).

A. Scanning

Only an overview of the scanning process and details relevant to the topic of this study are presented here. Specifically we are interested in identifying possible biases in the data sample and in the determination of the microbarn equivalent and four-prong cross-section in order to be able to determine cross-sections for observed processes. Further information may be obtained from previous reports.[8]

The approximately 41,000 pictures taken consist of eight rolls of film, numbered 24-31. Scan information presented here is based on an analysis of rolls 25-31, which comprise a total of 40,337 pictures. Approximately sixty percent of the film was scanned at Florida State University and forty percent at Fermilab.

Twenty-one percent of the frames were rejected because there were not at least two good views or there were more than fifteen tracks entering the defined fiducial volume. This left 31,770 good frames. For

each of the good frames, the following information was recorded:

- Beam count
- The location and prong count of all primary interactions in the fiducial volume
- The location and prong count of all secondary interactions that occur within ≈ 80cm. of the primary vertex
- Kinks
- Neutral particle decays
- $\pi\mu e$ decays
- Stopping and non-stopping protons
- Dalitz pairs

Beam tracks were defined as tracks entering the fiducial volume before interacting, with an angular deviation not greater than ± 2 milliradians from nominal. Protons were defined as positive tracks having an ionization at least two times that of the beam track. Dalitz pairs were included in the prong count and their existence was recorded separately.

The total interaction path length was calculated using[9]

$$L_{int} = (f\ N_o)\ \frac{m}{\rho\sigma}\ (1 - e^{-\frac{\rho\sigma}{m}\ x_{max}})$$

where L_{int} = total interaction path length = $2.62 \pm .04 \times 10^7$cm

f = fraction of π^- in beam   = $.960 \pm .007$

N_o = beam count   = 109,884

m = mass of hydrogen atom   = 1.673×10^{-24} g

ρ = density of hydrogen   = $.0635 \pm .0006$ g/cm^3

σ = total cross-section   = $24.60 \pm .05$ mb   [10]

x_{max} = fiducial volume length   = 281 ± 2 cm

Using this value for L_{int}, the microbarn equivalent has been determined from[9]

$$\text{Microbarn equivalent} = \frac{(\rho)\ (L_{int})}{m} = 1.00 \pm .02 \text{ events/}\mu b.$$

A total of 3037 four-prong events were observed. A number of additions and subtractions must be made to this raw number in order to correct for various deficiencies in the scanning process. Further detail about these corrections may be found in Reference 9, from which the following summary is derived.

Odd multiplicity events

Sixty-eight three-prong events were observed. These are all assumed to be four-prong events with an unobserved low-momentum proton.

Odd-multiplicity events with nine or more prongs are assumed to be the result of unresolved secondary interactions. These events are reduced in multiplicity according to the probability of producing 2, 4, or 6-prong secondary interactions. There are an estimated 14 ± 4 events missing from the observed four-prong sample due to this source of error.

Dalitz pairs

The number of γ-ray conversions (which result predominantly from π° decay) found and relevant scanning efficiencies indicates that there are 12 ± 3 events in the observed four-prong sample that are actually two-prong events with a Dalitz pair ($\gamma e^+ e^-$ decay mode of the π°). In addition there are an estimated 24 ± 5 events missing from the observed four-prong sample which have been misidentified as six-prong events.

Hidden γ-conversions

Gamma rays which convert near the primary vertex may be unidentified causing an incorrect prong count. The total number of missing gamma rays has been estimated by determining the distribution at inter-

mediate distances from the vertex, where the scanning efficiencies for gamma-ray conversions can be more accurately estimated, and extrapolating back to the vertex. There are an estimated 81 ± 10 two-prong events with a hidden γ-ray conversion in the sample, and an estimated 184 ± 14 four-prong events, misidentified as six-prong events, missing from the sample.

Hidden neutral strange particles

As in the case of hidden gamma conversions, hidden neutral strange particle decays cause an increase of +2 in the prong count. To correct for this error, the number of neutral strange particle decays is plotted as a function of the "linearized lifetime", $Q(\ell)$, defined by

$$Q(\ell) = \frac{\int_0^\ell e^{-x/\beta c \gamma \tau} \, dx}{\int_0^{\ell max} e^{-x/\beta c \gamma \tau} \, dx}$$

where x = distance to decay

ℓmax = maximum path length for a given event

$\beta c \gamma \tau$ = mean decay distance

The plot should be flat and losses are estimated on that basis. The four-prong sample has been found to be contaminated by an estimated 52 ± 7 two-prong events with a hidden neutral strange particle decay and to be missing 62 ± 8 events misidentified as having six-prongs.

Scanning efficiencies

A second scan was performed on 15% of the film to obtain efficiencies. All discrepencies between the two scans were resolved by a third scan. The relevant efficiencies obtained for four-prong primary vertices are:

ε_f = probability for finding a vertex = .919 ± .005

ε_i = probability that a vertex was classified correctly = .943 ± .004

Taking into account all the above sources of error, the corrected number of four-prong events is estimated to be 3328 ± 79 events, which corresponds to a topological cross-section of 3.32 ± .10 mb.

B. Measuring

A total of 1292 of the four-prong events (corresponsing to 42% of the observed sample) were measured. These represent an unbiased sample of all observed four-prong events, selected only on the basis of which rolls were available for measuring, except for roll 28, frames 2189-7536 (105 events) and roll 29, frames 4958-6959 (60 events).[11] For these sections of rolls 28 and 29 only events with no visible neutral decays (four-constraint fit candidates) were measured. In order to correct for this bias, the ratio

$$\frac{(\text{\# of events with vees})}{(\text{\# of events without vees})} = \frac{460}{667} = .690$$

was determined using the unbiased measurements. Then a weight factor, W, was used on the events with vees so that the above ratio remained the same for the sample of all measurements.

$$\frac{W* \ (\text{\# of events with vees})}{(\text{\# of biased and unbiased events without vees})} = .690$$

$$\frac{W \ (460)}{667 + 165} = .690$$

$$W = 1.25$$

This weight factor has been employed in all histograms presented in this study unless otherwise indicated.

All measurements were performed using the semi-automatic measuring machine (SAMM) at Fermilab. 435 of the measurements (Experiment 24, track matched) were done in 1975. The remaining 857 (Experiment 59, unmatched) were done in 1977. Vertices were measured only once (if visible) in each view. The vertex coordinates were then inserted as the first point of each track eminating from that vertex. The format of the measurement tape, as well as some special procedures necessary to read it are detailed in Appendix A.

A track code was assigned to each track. For track-matched events these codes were recorded only once for each track; for unmatched events a track code was recorded separately for each track-view. Track code definitions appear in Table III-1.

A sample bubble chamber photograph is shown in Figure III-2. The poor contrast and confusing, cluttered exposure are not atypical of the data. The raw measurements shown in Figure III-3 correspond to the four-prong event in Figure III-2. Note the large number of points measured per track, the large turning angle through which two of the tracks are measured, and the measurement of the beam track deep into the nose. These characteristics of the measurements created the need for some additional processing before the measurements could be successfully handled by TVGP. In addition many difficulties were experienced due to a large fraction of events with bad measurements (measured coordinates which do not correspond to the location of the track). These problems and the methods employed to deal with them are explained in more detail in section D of this chapter.

TABLE III-1

Track Codes

0	Not used
1	Track leaves; last point measured is a corresponding point
2	Stopping proton
3	Track interacts
4	Neutral two-point track (not applicable)
5	Track has kink
6	π-μ-e decay observed
7	Electron
8	Non-stopping proton
9	Last point measured is not a corresponding point
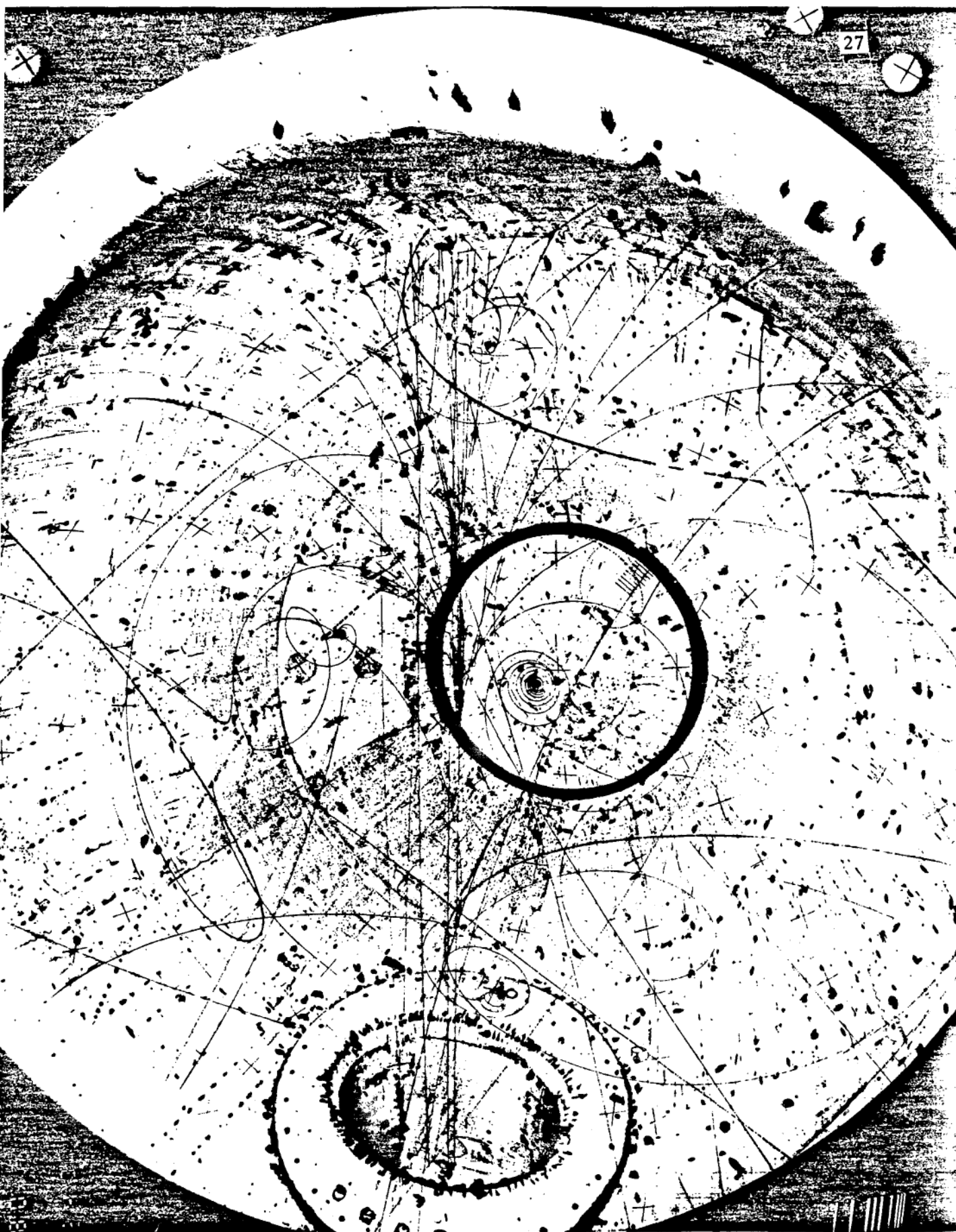
Figure III-2: Bubble chamber photograph. Four-prong event is on the right-most beam track, approximately half-way between the nose and the piston.
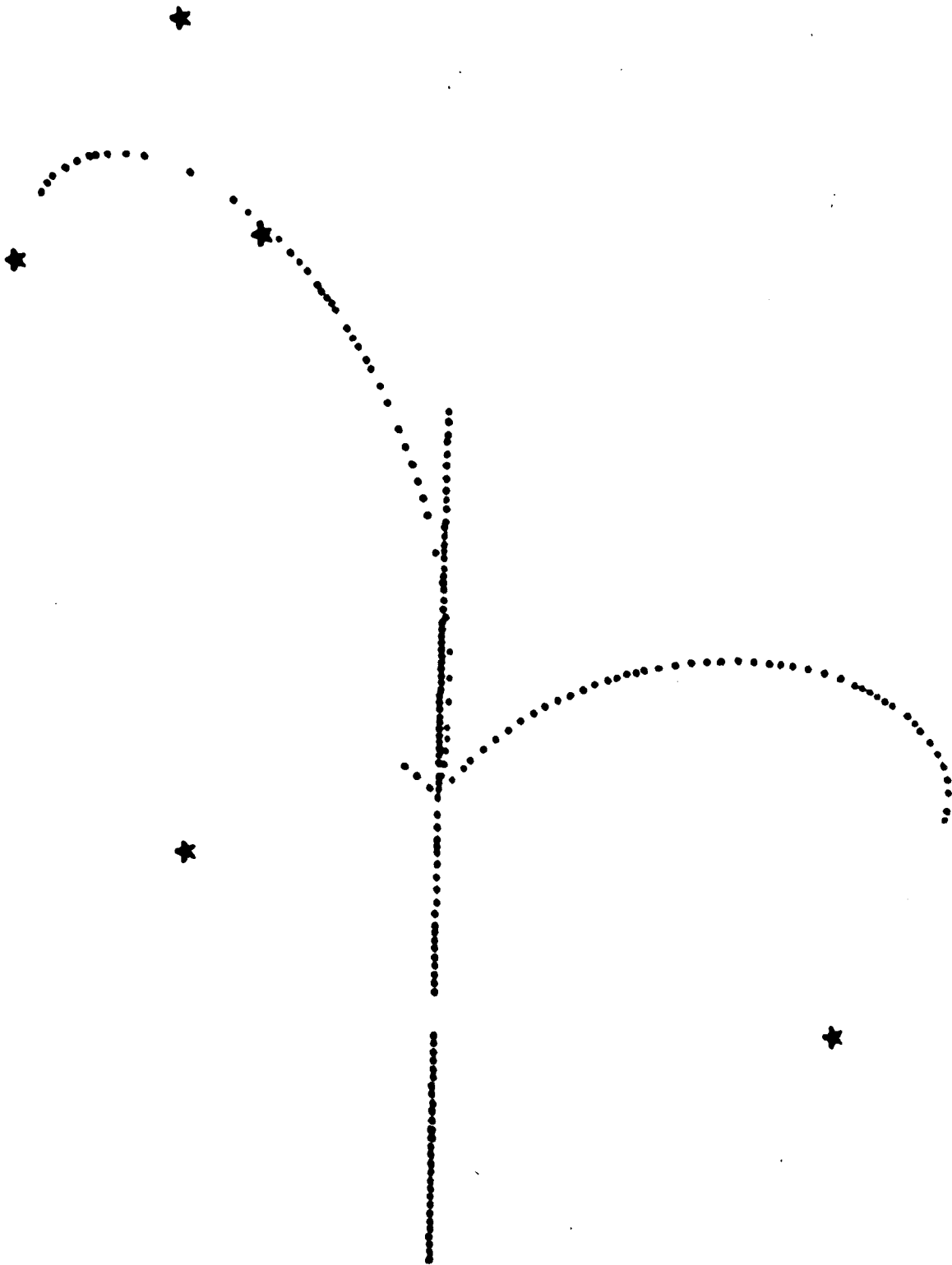
Figure III-3: Measurements of the four-prong event found in Figure III-1.

★ represent measured fiducials

• represent measured track coordinates

C. Pre-geometry Processing

In order for TVGP to be able to read the measurement tape, a computer program was created to rewrite the measurement tape in BRAVE output format. In addition, since TVGP can handle at most 40 measured points per track, the number of points per track was reduced by this program to a maximum of 39. For outgoing tracks with 40-49 (50-54) points every fourth (third) point was deleted, starting with the fifth (fourth) point from the end of the track until 39 points remained. This procedure insured a minimum of 4 or 3 consecutive original data points at the end of each outgoing track and 8 at the beginning.

The program also incorporated the capability of selectively deleting any number of points from the ends of particular tracks. This capability was employed after initial TVGP processing in an attempt to save failed tracks which were either measured through too large a turning angle for TVGP to handle or had bad measurements for some reason. This aspect is discussed in more detail in section D of this chapter.

D. Geometric Reconstruction and Track-matching

Although a version of TVGP for the fifteen-foot chamber was already in use at the University of Maryland, changes in some subroutines were found necessary. The more significant of these changes, as well as some relevant aspects of the original form of the program, are now described.

- FIDVOL: The fifteen-foot chamber's fiducial volume is defined in this subroutine to be a sphere of radius 212 cm., centered at $X = Y = 0$, $Z = 250$ cm., with the top and bottom cut-off at $Z = 60$ cm. and $Z = 440$ cm., respectively. Tracks which reconstruct outside

these limits are failed. All measured points for the beam track which correspond to X < 200 cm. (i.e. points in the nose of the bubble chamber) were deleted. In addition the first point of the beam track in view 1 was found to reconstruct inaccurately and was also deleted.

- TYPSUB: Typsub sets up the mass interpretations to be assigned. All secondary tracks, regardless of identification information (i.e. track codes) provided by the measurer, were tried as pions, protons, stopping protons, and kaons.

- USER: This subroutine sets various parameters of the bubble chamber. A film setting error of 10 microns was used. Floors on azimuth and slope errors were set at .05 degrees and .1, respectively. The criterion used for calling a momentum unmeasurable was $\Delta p/p > .5$. This criterion was later tightened in SQUAW to $\Delta p/p > .25$.

- CIRCLE: This subroutine fits the measured points in a view to a circle prior to space reconstruction. The resultant residuals and their standard deviation is calculated. Since the measured points may not fit a circle very well, the individual residuals are compared to four times the standard deviation of all the residuals. Individual measurements whose residuals exceed this limit are deleted and the fit is recomputed. It was found desirable to loosen this criterion by a factor of two for the first and last measured points for all tracks.

• SPFIT: Spfit does a least squares fit of the reconstructed measured
points to a track in space. After determining the fitted track
parameters, it calls AUX which calculates corrections to these
quantities. These corrections had been limited to 10 times the
expected error, with the result that many iterations in the fitting
procedure were required to converge to an acceptable solution. This
limit has been removed, resulting in the great majority of tracks
reaching a solution after only one or two iterations.

The MATCH program used for this study was also derived from an
existing version. It is based on the fact that in zeroth order optics
(indices of refraction of all optical components between the track and
the film are equal to 1), if the film plane is parallel to the camera
plane, the triangle formed by the measured positions of a point in three
views is similar to the triangle formed by the cameras, as illustrated
in Figure III-4. For each triad (combination of one track from each
view), the quantity ε is evaluated, where

$$\varepsilon \equiv ab - \left(\frac{AB}{AC} \right) ac$$

Here ab and ac are two legs (which meet at a particular point on one of the
track-views of the triad) of the triangle on the film plane and AB, AC
are the corresponding legs of the triangle formed by the cameras.
This quantity is then averaged over all points for which corresponding
points can be found in the other views. The average value of ε, called
RAT, is then used to evaluate and compare various triads. The smaller the
value of RAT, the more likely the triad is judged to be correct.
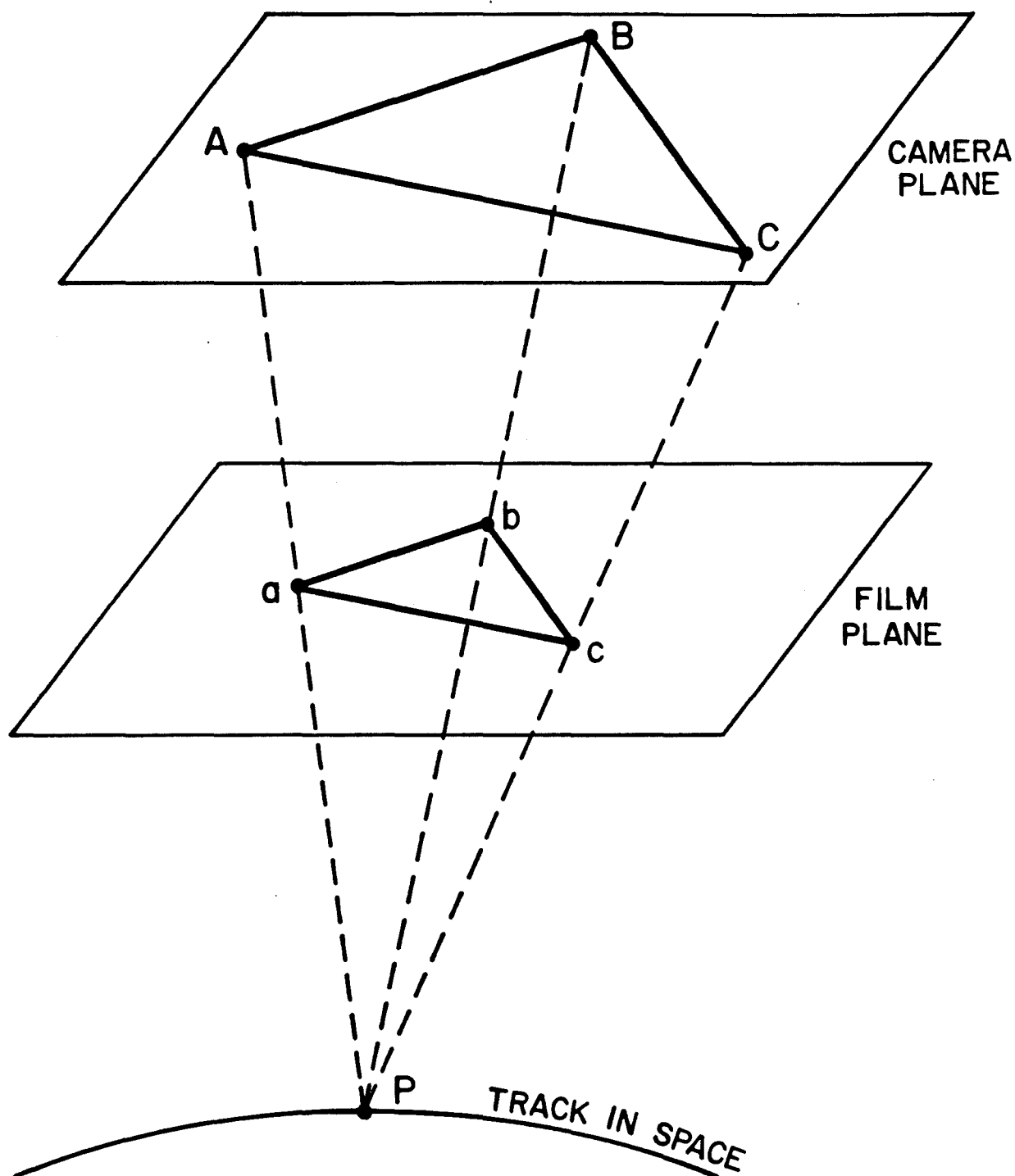
Figure III-4: Diagram illustrating the triangle formed by the measured positions of a point in three views is similar to the triangle formed by the cameras, provided the film plane is parallel to the camera plane.

Before RAT was calculated, an effort was made to limit the number of triads considered by requiring charge balance at the vertex. First the signed sagitta of each track-view was calculated and (if this sagitta was larger than a defined minimum), a charge was thereby assigned. Charge balance was then tested separately in each view. For those views which were not charge balanced, all charge assignments were removed. Then only those triads which had consistent charge assignments in each view were formed.

In an attempt to further eliminate unlikely triads from consideration, only those consistent with the track codes were used. For track codes 2 through 8, if this code appeared the same number of times in each view, triads which contained a track-view with this code were required to have all three track-views with this code.

It was found that short track-views would often have acceptable RAT's when combined in triads with much longer track-views, and not necessarily have good RAT's when combined in triads with tracks of similar length. Therefore if there existed one and only one track in each view with fewer than 6 points, all triads which combined a track with fewer than 6 points and a track with more than 19 points were eliminated. Also RAT was set extremely small (to 10^{-10}) for triads which contained only track-views with fewer than 6 points.

An additional problem arose with those triads for which only a small number (1 to 3) of corresponding points were found. Then a low value of RAT was found to be an unreliable estimator of the correctness of the triad. Therefore for all triads, RAT was weighted by the factor

$$1 + 10^{(4 - WGT)} \, ,$$

where WGT is the number of points used in the evaluation of RAT.

For all triads which were left, the following test was performed. A triad must have a RAT less than FLIM or must have a RAT less than CONS * FMINN. In the latter case RAT must also not exceed FMAX4. Here

FLIM = .00001

CONS = 4.0

FMINN = minimum RAT for a track in a view

FMAX4 = .0004

All triads which passed this test on RAT were then combined into as many events solutions as logically possible. If no solution was found, the charge assignments for all track-views were removed, and the whole procedure tried again. If still no solution was found, FMAX4 was doubled, and redoubled if necessary. If still no solution was found, the default match solution (track 1 in view 1 corresponds to track 1 in view 2, etc.) was reported to TVGP.

An event was judged to have failed this phase of the analysis if one or more of the following conditions obtained:

- more than one match solution was found
- no match solution was found (i.e. the default solution was taken by necessity)
- for Experiment 24 events, the found match did not correspond to the default match
- one or more tracks failed TVGP for all mass interpretations
- charge balance did not exist at the vertex (except for three-prong events)
- there was a fiducial failure in TVGP
- the X coordinate of the vertex was less than -190 cm. This criterion guaranteed a minimum beam track length of approximately 10 cm.

All such failures, with the exception of those in the last two categories, were plotted on a Tektronix graphics terminal in an attempt to ascertain the cause of the failure and possibly rectify it. First the correct match was determined using MATCH output, TVGP output for the match(es) attempted, the plotted track coordinates, track codes and, if necessary, the film. This was a relatively straightforward, unambiguous task except for the following problem. It was found that a significant fraction of the multiple matches were due, not to a problem with the MATCH program itself, but to the fact that the same track was measured twice in a view instead of two close, but distinct, tracks. Most of the time it was not possible to determine which track was measured, and sometimes the measurements could not uniquely be assigned to either track. That is, the measurements kept hopping back and forth between the two tracks. Figure III-5[12] is an example of this particular phenomenon involving three tracks.

In order to rectify this problem to the extent possible the following procedure was used. If distinct tracks were measured for the pair in question in two views and either duplicate tracks (one track measured twice) or mixed tracks (both tracks have measurements corresponding to the location of both real tracks, as in Figure III-5) were measured in the other view, then the measurements of the problem tracks in the bad view were simply eliminated. Of course if this problem existed in two or more views, this procedure could not be followed. In that case the plotted measurements were compared with the film. Occasionally it was possible to determine which track was the one actually measured. More

vertex
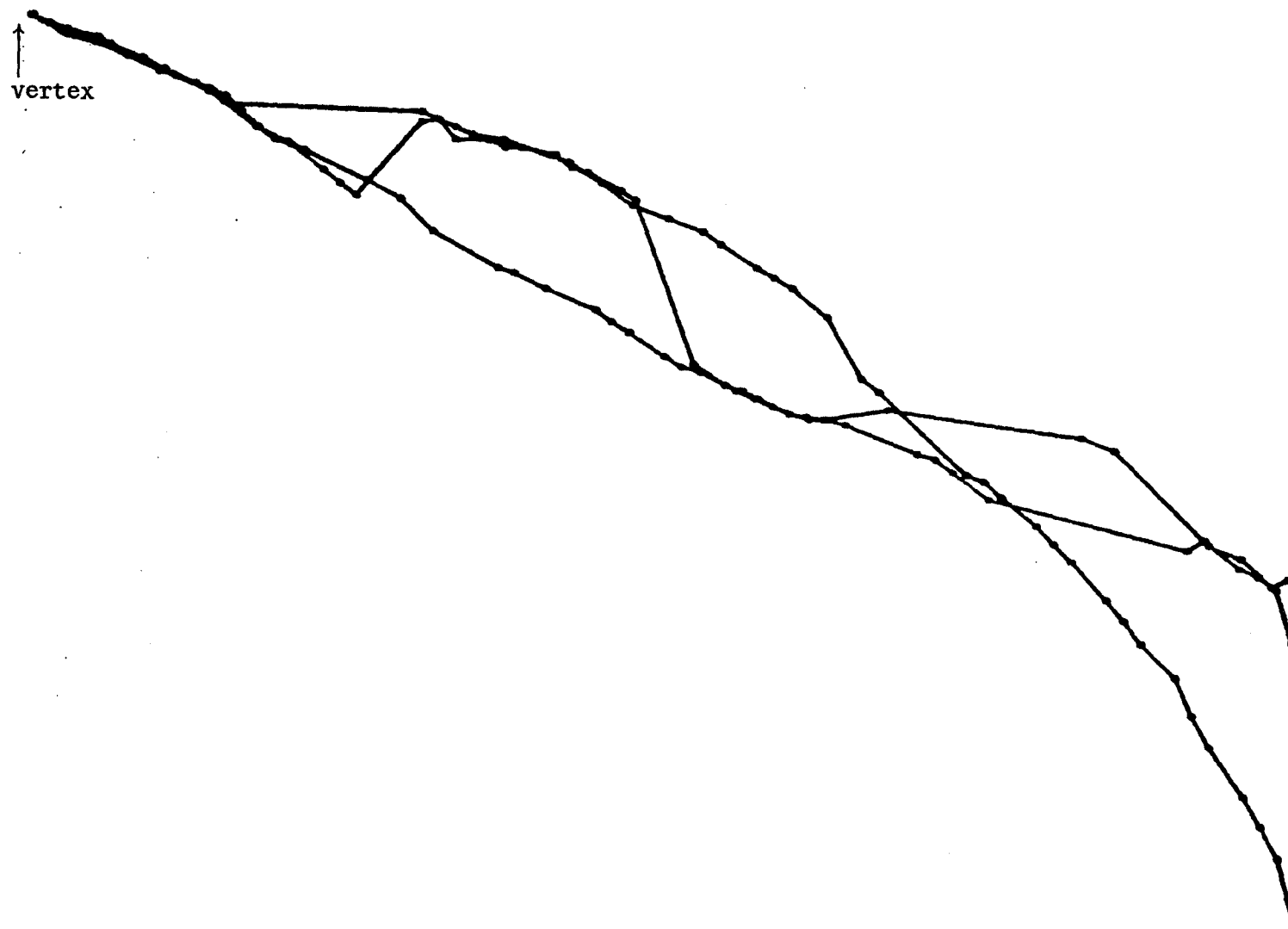
Figure III-5: Bad measurements on three closely spaced tracks. Vertical scale has been
expanded for clarity.

often, it was necessary to cut back on the track measurements to the region where they overlapped on the film.

To estimate the number of incorrect matches contaminating the data sample, the Experiment 24 events have been examined. It is assumed that if one and only one match solution was found, and if it is equivalent to the default match, and if there were no TVGP problems with the event, then the found match is the correct match. For all other Experiment 24 events, the found match was determined by hand as previously described, and it is also assumed that there is no error in this procedure. A total of 7 events were found for which there was one and only one match solution (which did not correspond to the default solution) and the event passed TVGP. Of these, 2 were determined to have an incorrect found match. This number is used to estimate the number of false matches in the Experiment 59 events, since false matches are assumed to be only among Experiment 59 events, which similarly had only one match solution with no TVGP problems. (All other Experiment 59 events have been matched by hand.) Thus, scaling up to the number of Experiment 59 events, there are an estimated 4 incorrect matches in the final data sample.

After the match for an event was determined, track failures were examined. Some were caused by the measurement of a track through too large a turning angle for TVGP to handle, as described in section III-2 and illustrated in Figure III-3. These were easily saved by cutting back on the track. Others were caused by bad measurements of a track in one or more views. If this occurred near the end of a track, only part of the track measurements were eliminated. However a significant fraction of the time the entire track-view had to be eliminated (Figure III-6).[12] Sometimes an entire view had to be eliminated (Figure III-7).[12]
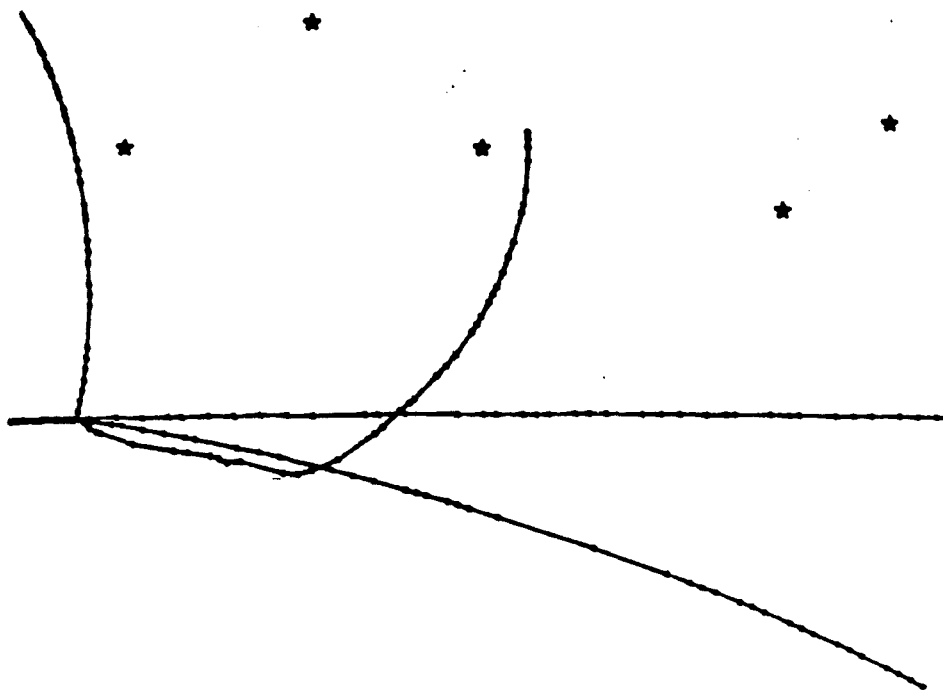
Figure III-6: A badly measured track; entire track has been deleted in this view.
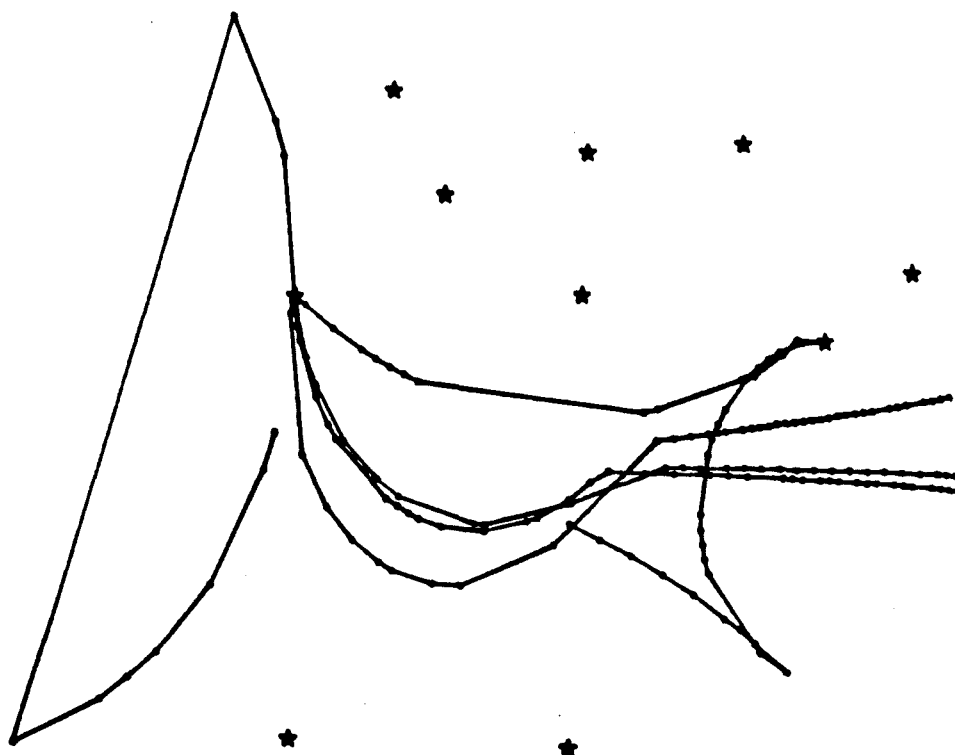
Figure III-7: A badly measured view; entire view has been deleted.

The final result of this phase of the analysis is that, of the 1292 measured events,

17   had MATCH failures,

50   had TVGP failures,

38   had X coordinate of the vertex less than -190 cm.

Excluding the last category, this represents a net failure rate of 5.3%. With the weight factor described in section III-B, the total number of events represented by the final sample is 1293.5.

E.   Kinematic Fitting

Fits to the primary vertex of the hypotheses

$$\pi^- p \rightarrow \pi^- \pi^+ \pi^- p$$

$$\pi^- p \rightarrow \pi^- \pi^+ \pi^- p_{stopping}$$

were attempted.. All positive tracks which passed the TVGP proton (stopping proton) hypothesis were tried as protons (stopping protons). However, for those events in which a proton was identified by the measurer, fits which did not correspond to that information were later rejected (in SUMX).

For three-prong events (with an assumed missing short proton), the proton was assigned with momentum components of

$$P_x = 0 \pm 40 \text{ MeV/c}$$

$$P_y = 0 \pm 40 \text{ MeV/c}$$

$$P_z = 0 \pm 50 \text{ MeV/c.}$$

All fits used a beam momentum of 250 ± 1 GeV/c.

F. DST Preparation

DST preparation was accomplished using a modified version of an existing program, ARROW. No attempt at particle identification was attempted in this phase of the analysis; track banks for all mass hypotheses appear on the DST. These track banks include track codes passed through TVGP and SQUAW, TVGP-generated geometry information, and parameters of interest (rapidity, Feynman X, etc.) calculated in ARROW. Similarly fit blocks for successful fits contain both SQUAW-generated fit information as well as parameters of the fitted tracks calculated in ARROW. The format of the SDT is described in APPENDIX B.

G. SUMX

SUMX was used to generate lists, histograms, and diplots from the DST. In addition, event selection, track identification, and the bulk of the physics calculations were performed using this program. Modifications were made to increase the buffer size to 6000 words and to increase the maximum number of entries per event to 10 for histograms (BLOC10) and to 9 for diplots (BLOC11).

CHAPTER III

References

1. F.J. Solmitz, A.D. Johnson, J.B. Day, "Three-View Geometry Program" LRL Alvarez Group Programming Note P-117, 2nd Ed. (June 20, 1966).

    T.B. Day, "TVGP-SQUAW (Md. Version)..Operational Information", University of Maryland Department of Physics and Astronomy Technical Report No. 649 (December, 1966).

    B. Kehoe and D.G. Hill, "TVGP and SQUAW changes at Md. 1969 to December 1963", University of Maryland Department of Physics and Astronomy Technical Report No. 75-005 (June, 1974).

    D.G.Hill, "TVGP and SQUAW changes at Md. January 1, 1975 - January 1, 1976", University of Maryland Department of Physics and Astronomy Technical Report No. 76-093 (March, 1976).

    R.G. Glasser, "Changes to TVGP and SQUAW since TP76", University of Maryland Department of Physics and Astronomy TPSQ-1, HEP-25 (2/28/76).

2. R.K. Böck, CERN/D.Ph. II/Prog 74-4, 24.5 1974 (unpublished).

3. R.G. Glasser, "BRAVE--University of Maryland TVGP Preprocessor", University of Maryland Department of Physics and Astronomy Technical Report No. 73-091 (February, 1973).

4. W. Manner, "Track Matching in Bubble Chamber Geometry Programs", Argonne National Laboratory POLLY Note No. 18 (March 1968).

    R.G. Glasser, "ANL MATCH Program Short Description", June 29, 1972 (unpublished).

    "Match Revisions", University of Md. High Energy Physics Memo HEP-15.

5. O.I. Dahl, T.B. Day, F.T. Solmitz, N.L. Gould, "SQUAW Kinematic Fitting Program", LRL Alvarez Group Programming Note P-126 (July, 1968).

6. G. Thompson, "Operating Instructions for ARROW 35", High Energy Physics Memo, University of Maryland (May, 1976).

7. D.E. Trevvett, "SUMX Version M-5", University of Maryland Department of Physics and Astronomy Technical Report No. 75-038 (December, 1974).

8. S. Hagopian, J.R. Albright, P. Hays, and J.E. Lannutti, Florida State University Report No. FSU-HEP-76-1-02, 1976 (unpublished).

9. P.J. Hays, R.N. Diamond, R.K. Clark, S. Hagopian, J.E. Lannutti, J.P. Berge, D.Bogert, R. Hanft, R. Harris, F.R. Huson, S. Kahn, and W. Smart, Florida State University Report No. FSU-HEP-79-18-12, 1979 (submitted to Phys. Rev.).

10. A.S. Carroll et al., Phys. Lett. 61B, 303 (1976), as referred to in 9, above.

11. S. Hagopian, private communications, 1979 and 1980.

12. In Figure III-4, III-6, and III-7, the horizontal and vertical scales are not equal in order to obtain maximum detail.

CHAPTER IV

PHENOMENOLOGICAL CHARACTERISTICS OF FOUR-PRONG $\pi^- p$ INTERACTIONS

In this chapter some phenomenological features of the data are examined by analysis of single particle inclusive distributions and the recoil from the proton. As mentioned in chapter III, all particles are assumed to be pions unless identified as protons using the track codes.

A substantial number of the particles were too straight for an accurate ($\Delta p/p <$ .25) momentum determination. These are hereinafter referred to as LSN3 tracks, following TVGP terminology. For identified stopping protons the momentum was determined from the range of the track rather than the curvature; these are LSN1 tracks. The remainder of the tracks, for which momentum was determined from curvature, are referred to as LSN0 tracks. The total number of each type of particle with each LSN code is shown in Table IV-1.

There are a total of 420.75 LSN3 tracks. These represent 1.6% of the identified protons, 5.4% of the π^+, and 11.6% of the π^-. The 420.75 LSN3 tracks are distributed among the 1293.5 events as follows:

935.75 events have 0 LSN3 tracks,

301.5 events have 1 LSN3 track,

49.5 events have 2 LSN3 tracks,

6.75 events have 3 LSN3 tracks.

TABLE IV-1

SINGLE PARTICLE LSN CODE SUMMARY

Particle		Number	
Protons			
	not seen	33.0	
	LSN0	91.25	
	LSN1	370.75	
	LSN3	8.25	
		503.25	total
π^+			
	LSN0	1971.25	
	LSN3	112.5	
		2083.75	total
π^-			
	LSN0	2287.0	
	LSN3	300.0	
		2587.0	total

A. Single Particle Inclusive Distributions

The specification of an n-particle final state requires 3n momentum components. It is difficult to analyze and/or display such data for n > 2. Therefore experimenters have developed an interest in inclusive reactions. These are reactions of the form

$$a + b \rightarrow c \ldots + X$$

where a = beam particle

b = target particle

c... = one or more specified reaction products

X = the remaining particles in the final state.

For this study the total number of charged particles is specified. Also, only single particle distributions are analyzed. Hence the appropriate semi-inclusive reaction in this experiment is

$$\pi^- p \rightarrow a^{\pm} + X^{\mp}$$

where $a^{\pm}$ represents π^-, π^+, or proton

$X^{\mp}$ contains 3 charged particles and an

unspecified number of neutrals.

Inclusive distributions in transverse momentum squared, Feynman X, and center-of-mass rapidity of partially integrated invariant differential cross-sections for π^-, π^+, and protons are presented in this section. The form of the invariant differential cross-section,

$$E \frac{d^3\sigma}{d\vec{p}} \qquad ,$$

where E and $\vec{p}$ are the energy and momentum of the observed particle "a", depends on the variables chosen for $\vec{p}$. If $\vec{p}$ is decomposed into longitudinal (with respect to the beam) and transverse components, and an integration is performed over the angle about the beam, then

$$E \frac{d^3\sigma}{d\vec{p}^3} = \frac{E}{\pi} \frac{d^2\sigma}{dP_L dP_T^2}$$

Various substitutions for P_L have been found useful.[1] Feynman X, defined by

$$X_F \equiv \frac{P_L^{cm}}{P_L^{cm} \, max} \simeq \frac{2}{\sqrt{s}} P_L^{cm}$$

is restricted to the range $-1 \leq X_F \leq 1$. Using this variable the invariant differential cross-section has the form

$$E \frac{d^3\sigma}{d\vec{p}^3} = \frac{2}{\pi\sqrt{s}} E^{cm} \frac{d^2\sigma}{dX_F \, dP_T^2} \qquad .$$

Rapidity, defined by

$$Y = \frac{1}{2} \ln \left(\frac{E + P_L}{E - P_L} \right)$$

is another common substitution for P_L. In the center-of-mass, the beam has a rapidity of 5.04 units and the target proton has a rapidity of -3.14 units. Thus a maximum rapidity gap of 8.18 units is available in this experiment. Although rapidity requires a momentum measurement, the pseudo-rapidity defined by

$$\eta = \lim_{P_T^2 \gg m^2} Y = \frac{1}{2} \ln \left(\frac{1 + \cos\theta}{1 - \cos\theta} \right) \qquad ,$$

where θ = angle between beam and particle, is often a good approximation to the rapidity.[2] For LSN3 particles the pseudo-rapidity has been used in rapidity distributions presented in this chapter. Using rapidity for the longitudinal momentum variable, the invariant differential cross-

section has the form

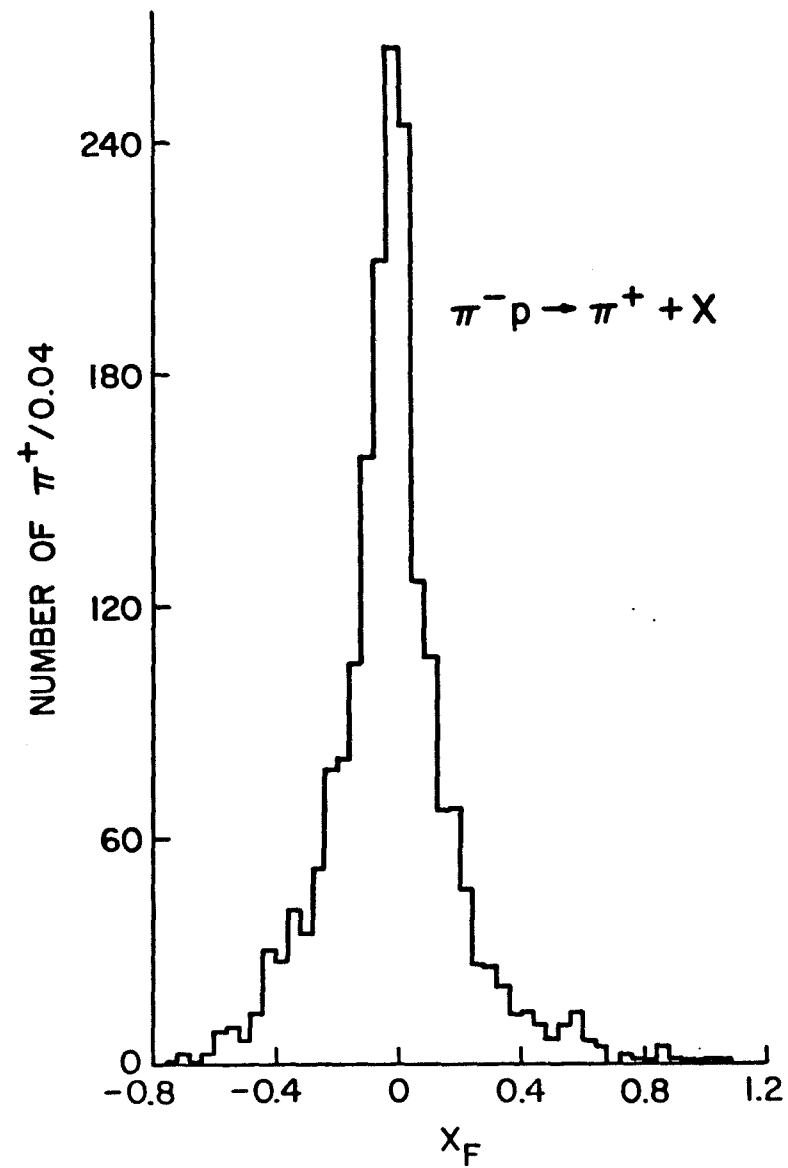$$E \frac{d^3\sigma}{d\vec{p}^3} = \frac{1}{\pi} \frac{d^2\sigma}{dY^{cm}dP_T^2} \quad .$$

The distributions of numbers of π^- and π^+ as a function of Feynman X are shown in Figures IV-1A and IV-1B, respectively. The corresponding invariant differential cross-sections integrated over P_T^2, $f(X_F)$, are shown in Figures IV-2A and IV-2B, respectively.

In comparing the π^- and π^+ distributions of Figures IV-1A and IV-1B, the major difference (aside from the total number of π^+ being fewer than the total number of π^-, due to proton identification) is the peak near $X_F = .8$ in the π^- distribution. The existence of such a peak has been interpreted as evidence for target diffraction.[3] In this model the target is diffracted to an excited state and the beam deflected, consistent with energy and momentum conservation. Subsequently the target decays into the other final state charged particles plus any neutrals. The deflected beam particle, or leading pion, has high center-of-mass momentum in the forward direction and is the source of the observed peak. The decay products from the excited state of the target are smeared in the Feynman X distribution at negative X_F with smaller average magnitude.

In Figures IV-2A and IV-2B the contribution of each particle to the cross-section has been weighted by its center-of-mass energy in order to get the invariant differential cross-section integrated over P_T^2, as shown. Thus we see a much more pronounced peak near $X_F = +.8$ in the π^- distribution (Figure IV-2A). The overall scales of Figures IV-2A and IV-2B are now quite dissimilar, reflecting a higher average center-of-mass energy of π^- particles compared with π^+ particles.
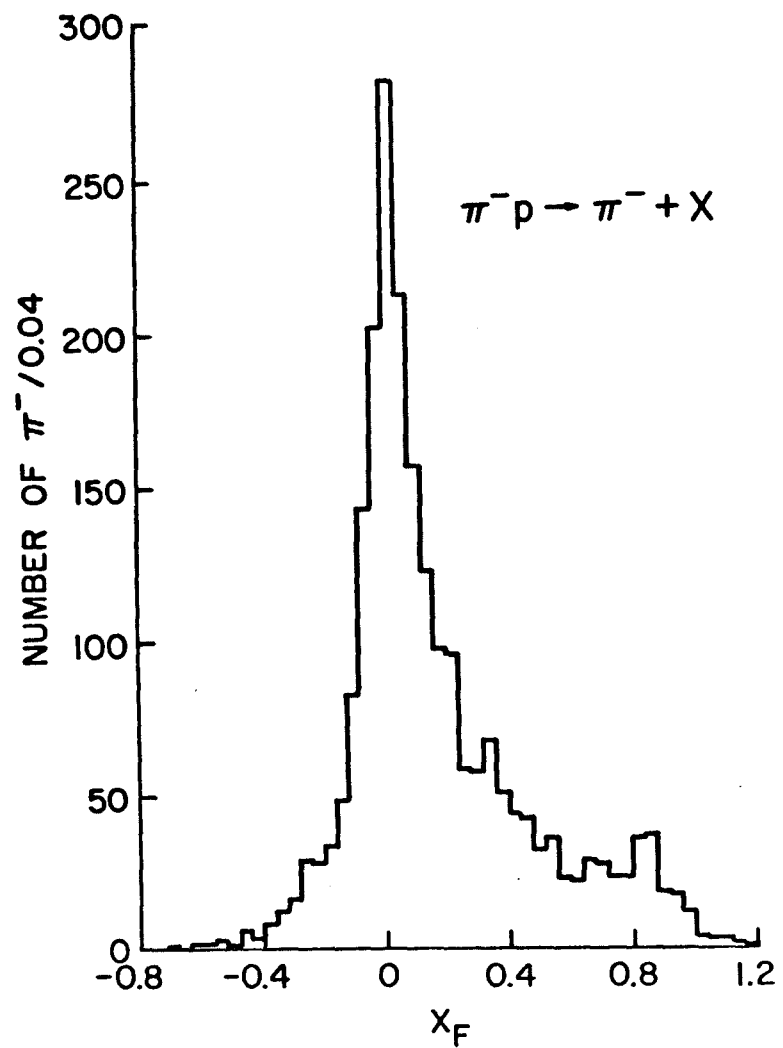
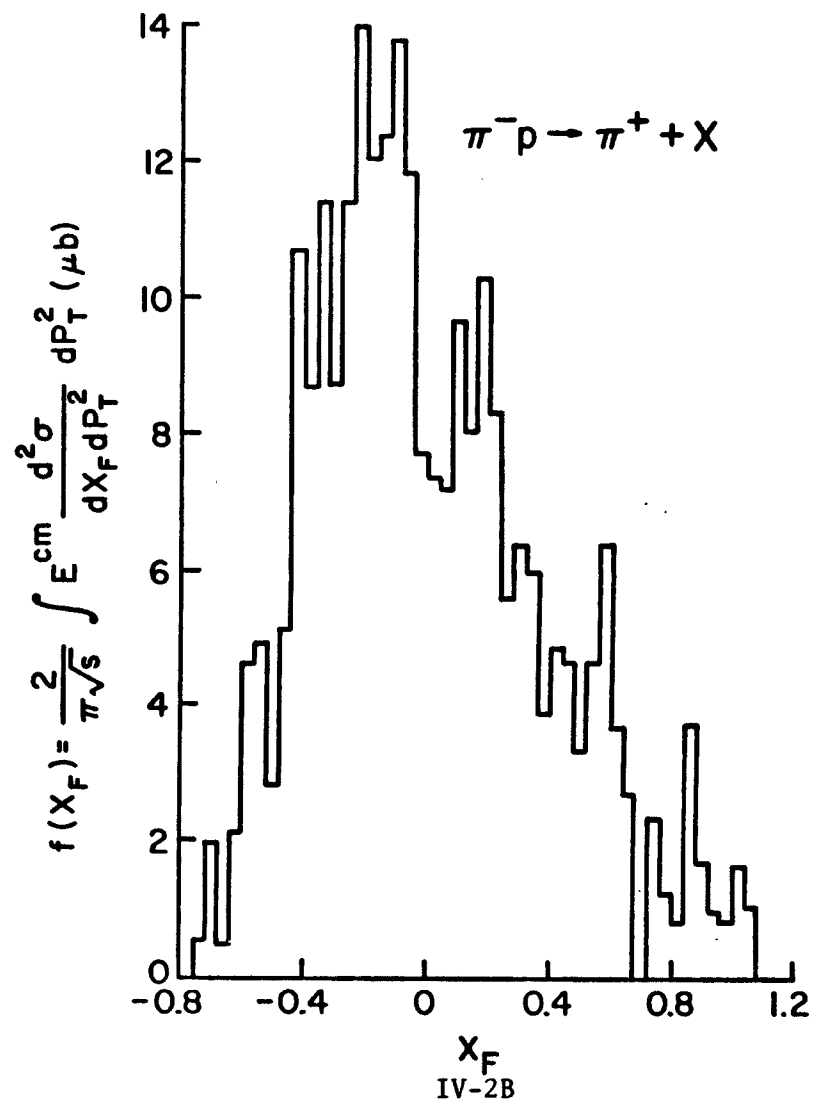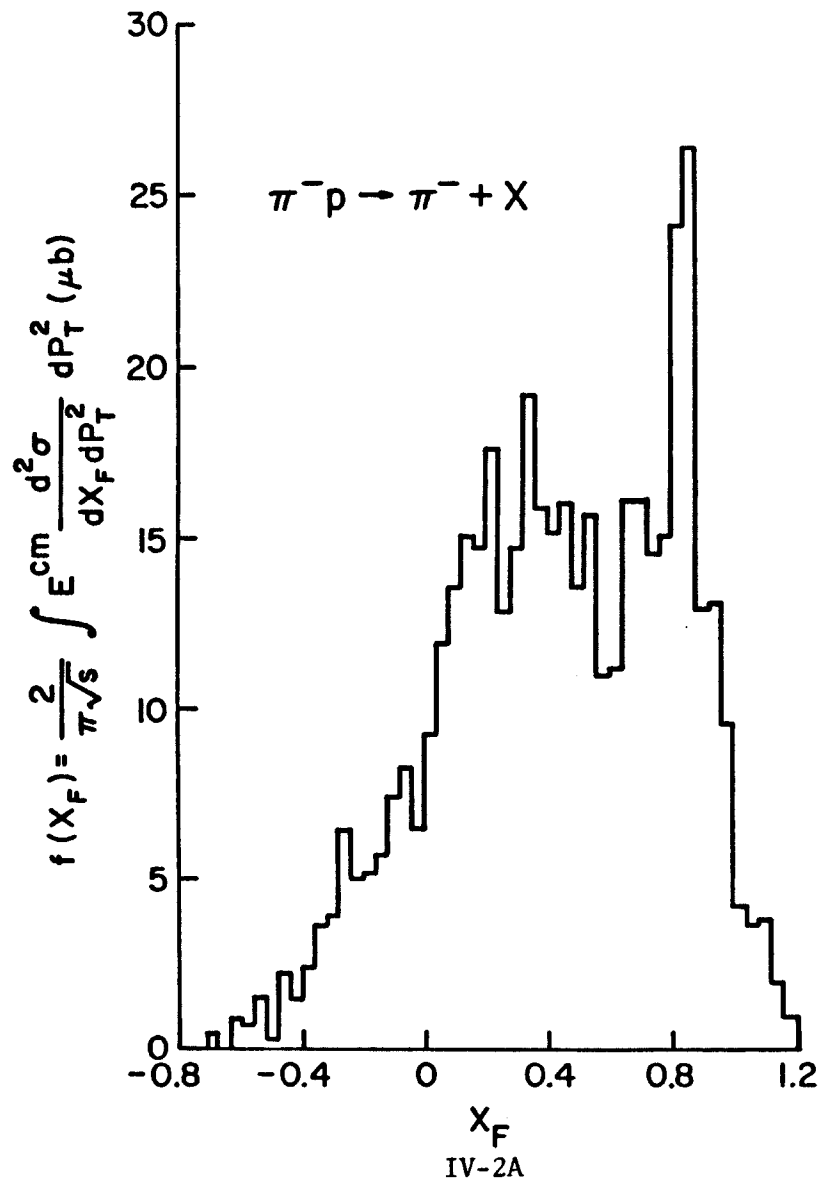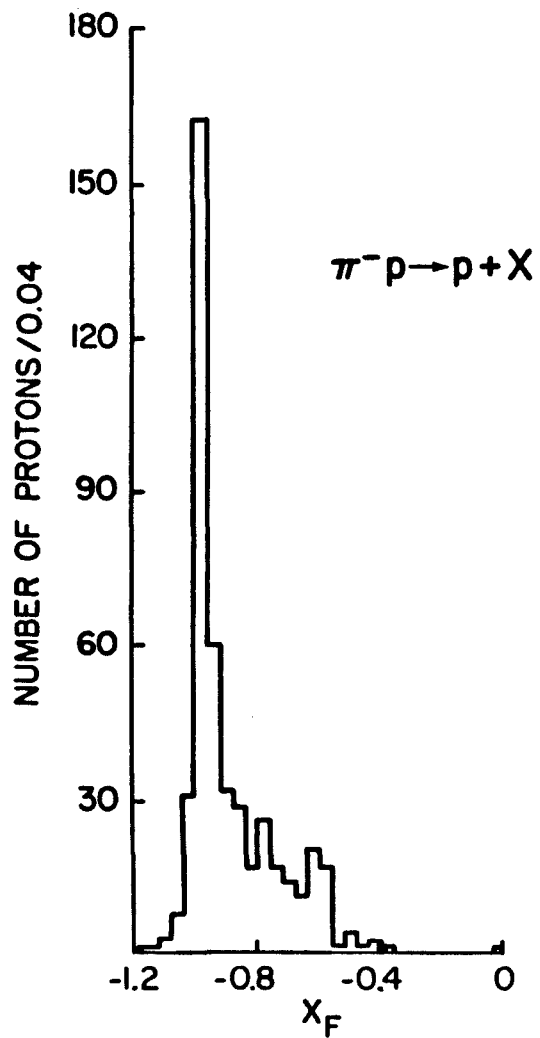Figure IV-1A, 1B: Feynman X distribution for π^-, π^+.

Figure IV-2A, 2B: Invariant differential cross-section integrated over P_T^2 (as a function of Feynman X) for π^-, π^+.

The distributions of numbers of protons and the invariant differential cross-section integrated over P_T^2 as functions of Feynman X are shown in Figures IV-3A and IV-3B, respectively. These distributions are not particularly informative since the accumulation of protons with large negative values of Feynman X can only be said to reflect the inability to identify by ionization protons with high laboratory momenta. There is little difference in shape between the two proton distributions.

The invariant differential cross-sections for π^-, π^+, and protons as a function of center-of-mass rapidity are shown in Figures IV-4A, IV-4B, and IV-4C, respectively. The π^- particles are seen to be produced predominantly in the forward direction in the center-of-mass, while the π^+ particles have a much more equal forward-to-backward distribution, with somewhat more being produced in the backward direction. The fact that neither of these distributions are dominated by centrally-produced pions may be taken as evidence for the dominance of diffractive or diffraction-like processes. Again, the proton distribution (Figure IV-4C) only reflects the fact that only low-momentum protons are identifiable.

The invariant differential cross-sections integrated over Feynman X, $g(P_T^2)$ for π^-, π^+, and protons are shown in Figures IV-5A, IV-5B, and IV-5C, respectively. The pion distributions are decreasing approximately linearly indicating an exponential function of P_T^2. The larger totals for the π^- distribution are due both to fewer π^+ particles and a higher average center-of-mass energy for π^- particles. The proton distribution is not clearly decreasing linearly, but is complicated by missing protons, unidentified protons, and lower overall statistics than the pion distributions.
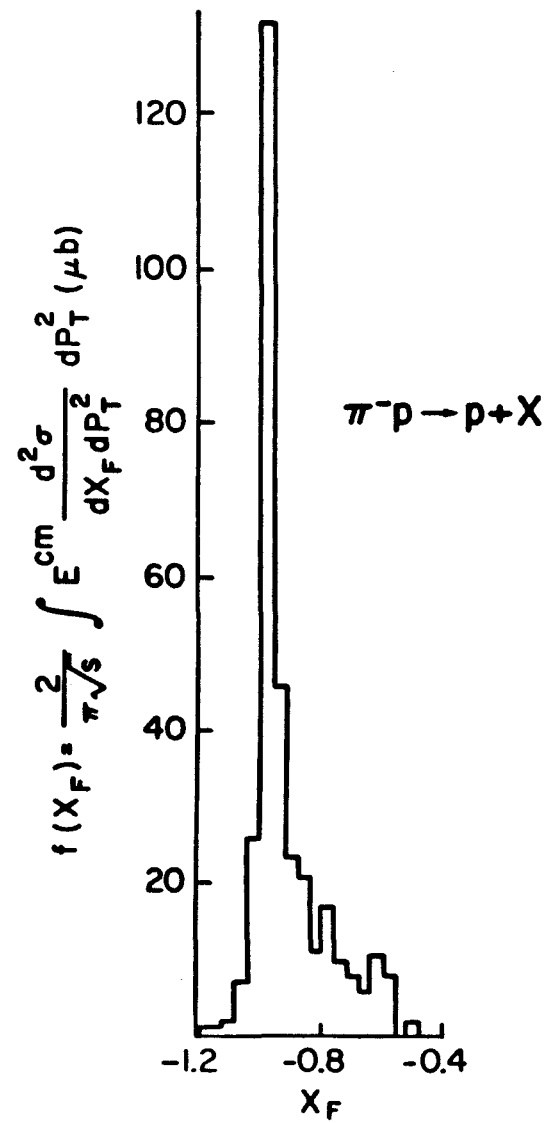
Figure IV-3A, 3B: Feynman X distribution and invariant differential cross-section integrated over P_T^2 (as a function of Feynman X) for protons.
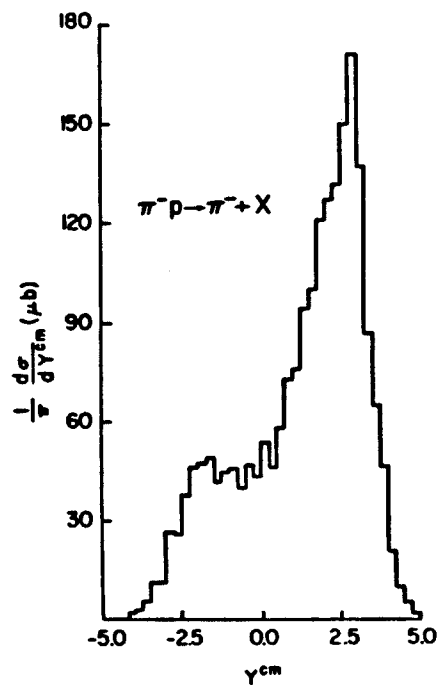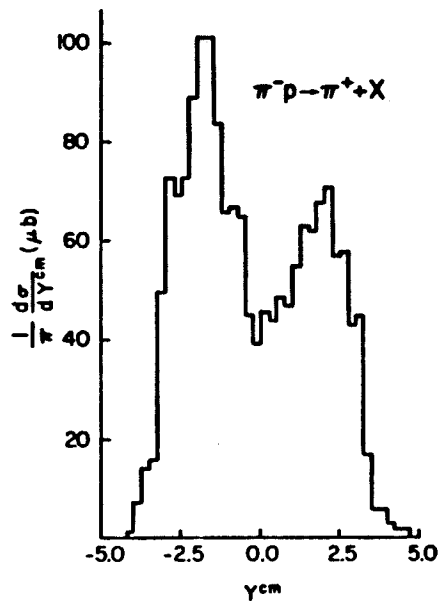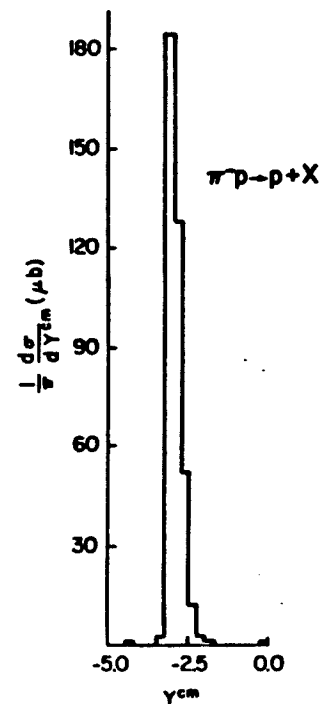
Figure IV-4A, 4B, 4C: Invariant differential cross-section integrated over $P_T{}^2$ (as a function of center-of-mass rapidity) for π^-, π^+, protons.
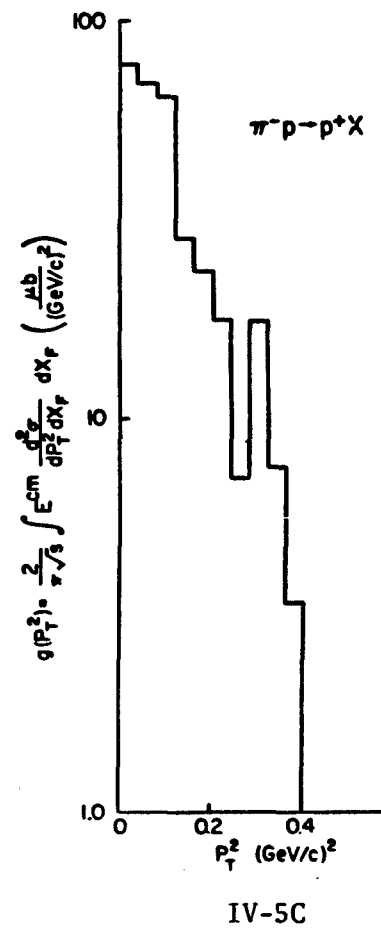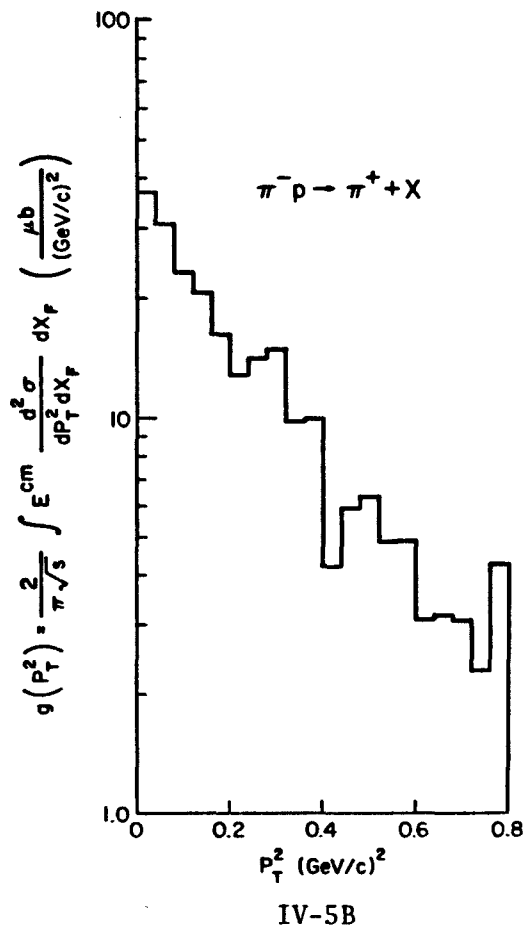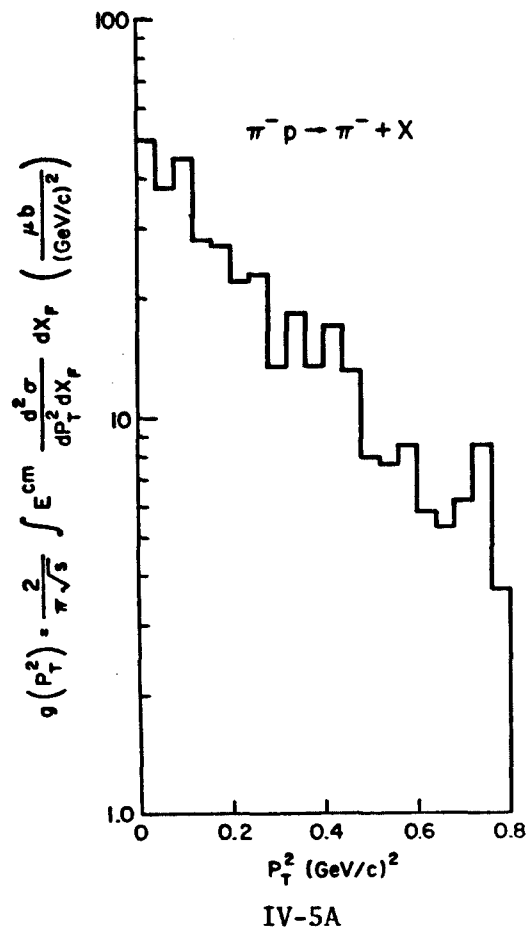
Figure IV-5A, 5B, 5C: Invariant differential cross-section integrated over X_F (as a function of transverse momentum squared) for π^-, π^+, protons.

B. Recoil From the Proton

In the inclusive reaction

$$\pi^- p \rightarrow p + X$$

the system "X" may also be investigated. In Figure IV-6, the distribution of effective mass squared of "X" is shown. There is a large dominant peak centered between 0 and 4 GeV^2, with a full width of approximately 16 GeV^2 and a shoulder extending to approximately 36 GeV^2. This peak provides evidence for substantial beam diffraction up to masses of $\sim$ 6 GeV, which is consistent with results achieved at 205 GeV/c.[5]
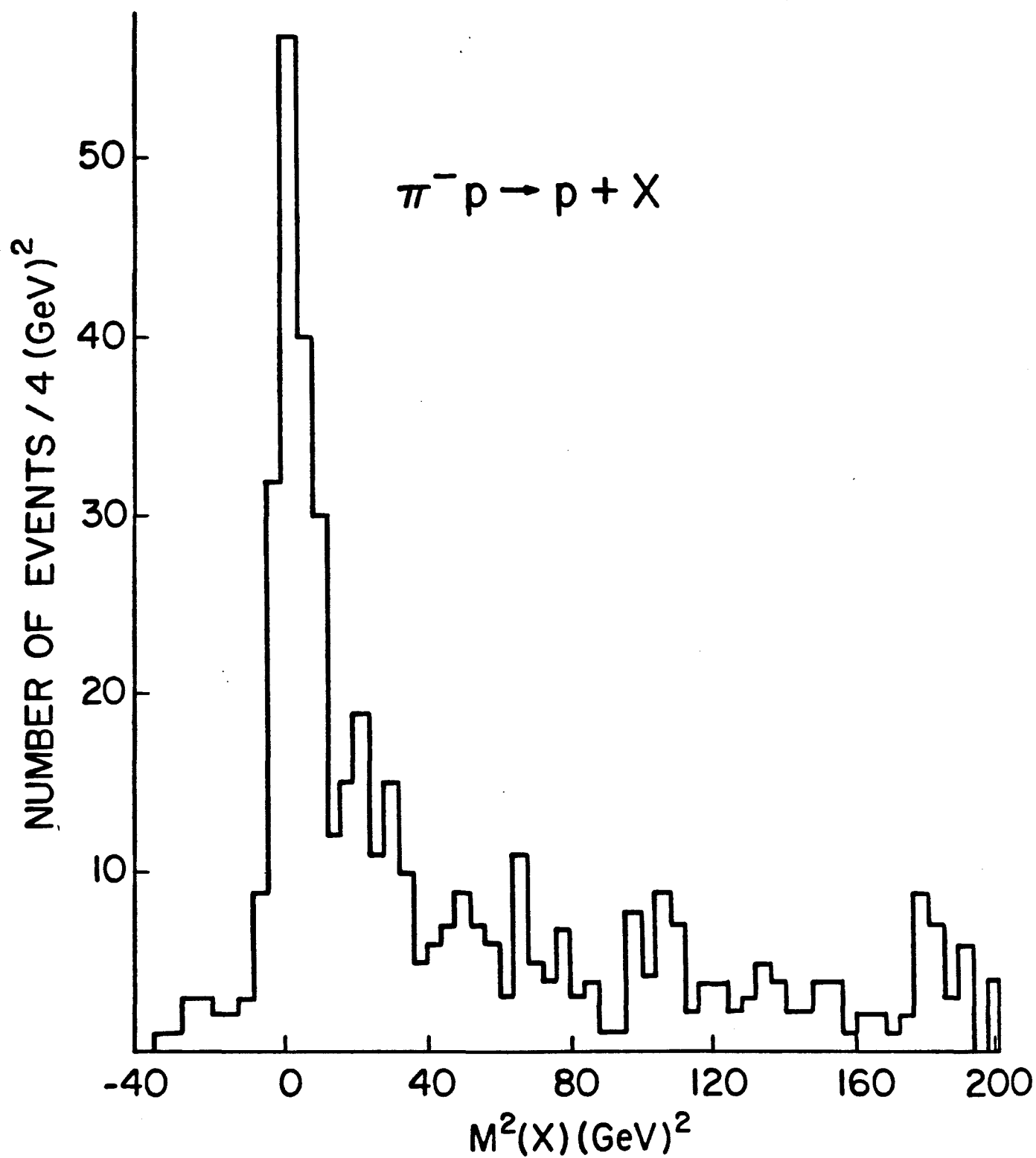
Figure IV-6: Effective mass squared of system recoiling from the proton.

CHAPTER IV

References

1. For a summary of these variables and their inter-relationships, see

    W.R. Frazer et al, Rev. Mod. Phys. 44, 284 (1972).

2. For example, for a pion with a longitudinal momentum of 10 GeV/c and

    a transverse momentum of .4 GeV/c the error introduced, $|\eta - Y|$, is .3.

    For a pion with a longitudinal momentum of 1 GeV/c and a transverse

    momentum of .1 GeV/c the error is .5. The approximation fails as

    $P_T \rightarrow 0$.

3. See, for example, W. Morris et al, Phys. Lett. 56B, 395 (1975).

4. For LSN3 particles, the pseudo-rapidity as defined previously in this

    chapter, has been used in Figures IV-4A, IV-4B, and IV-4C.

5. F.C. Winkelmann, et al, Phys. Rev. Lett. 32, 121 (1974).

CHAPTER V

RESONANCE PRODUCTION IN FOUR-PRONG $\pi^- p$ INTERACTIONS

Since resonances have lifetimes too short to leave a visible track or observable interval between the primary vertex and the resonance decay indirect means must be used to identify them. In this study the effective mass

$$M = [(\sum_{i=1}^{n} E_i)^2 - (\sum_{i=1}^{n} \vec{P}_i)^2]^{1/2}$$

is calculated for combinations of n observed particles with the expectation that resonances will manifest as signals in otherwise smooth distributions. The search encompasses those resonances which decay into $(\pi^+\pi^-)$, $(p\pi^\pm)$, $(\pi^+\pi^-\pi^\pm)$, and $(p\pi^-\pi^\pm)$ channels.

There are several difficulties in the application of this method to the data. As noted in chapter III, all tracks are taken as pions unless identified by the track codes as protons. Also it is difficult to determine the effect of the biases discussed in chapter III on the effective mass distributions. Most important, however, is the fact that there exists a substantial fraction of LSN3 tracks. The effective mass of a combination of particles involving an LSN3 track is not calculable; hence these combinations do not appear in the effective mass distributions presented.

Following are the results of the resonance searches for each of the channels studied.

A. $\pi^+\pi^-$

The effective mass distributions of ($\pi^+\pi^-$) pairs is shown in Figure V-1. Two methods were used in an attempt to simulate the background. The first method used the effective mass distribution of like-charged pion pairs, ($\pi^+\pi^+$) and ($\pi^-\pi^-$). However there are only approximately half as many entries in this distribution as in the ($\pi^+\pi^-$) distribution. This does not provide the necessary statistical accuracy for a background determination. The second method used oppositely charged pions from different events. Although the statistical accuracy was much better, the resultant effective mass distribution was found to provide a poor representation of the background. The background shown in Figure V-1 is hand-drawn.

There is a strong signal in the K°_S (.498 GeV) region, probably due to the K°_S decays which have been misidentified as secondary particles. However it is possible that part of this signal is due to the presence of Δ° (.53 GeV, with the proton misidentified as a pion). Smaller bin sizes have failed to resolve two peaks in this region.

There is another strong signal in the ρ°(.77 GeV) region. The signal above the hand-drawn background comprises 156 ± 32 events which correspond to a cross-section of .42 ± .09 mb. See Appendix C for details of this calculation. This represents a lower bound on the ρ° cross-section due to the unknown number of ρ°'s with an LSN3 track. This value is compared with previously published results at 100, 147, 205, and 360 GeV/c in Table V-1.[1,2] The results from this study show no significant deviation from the trend toward lower cross-section for ρ° production at higher energies.

There is an excess accumulation of events near 1.2 GeV, which may be due to the presence of the f(1.27 GeV). Except for this signal, there is no significant evidence of resonance activity at masses higher than that of the ρ°.

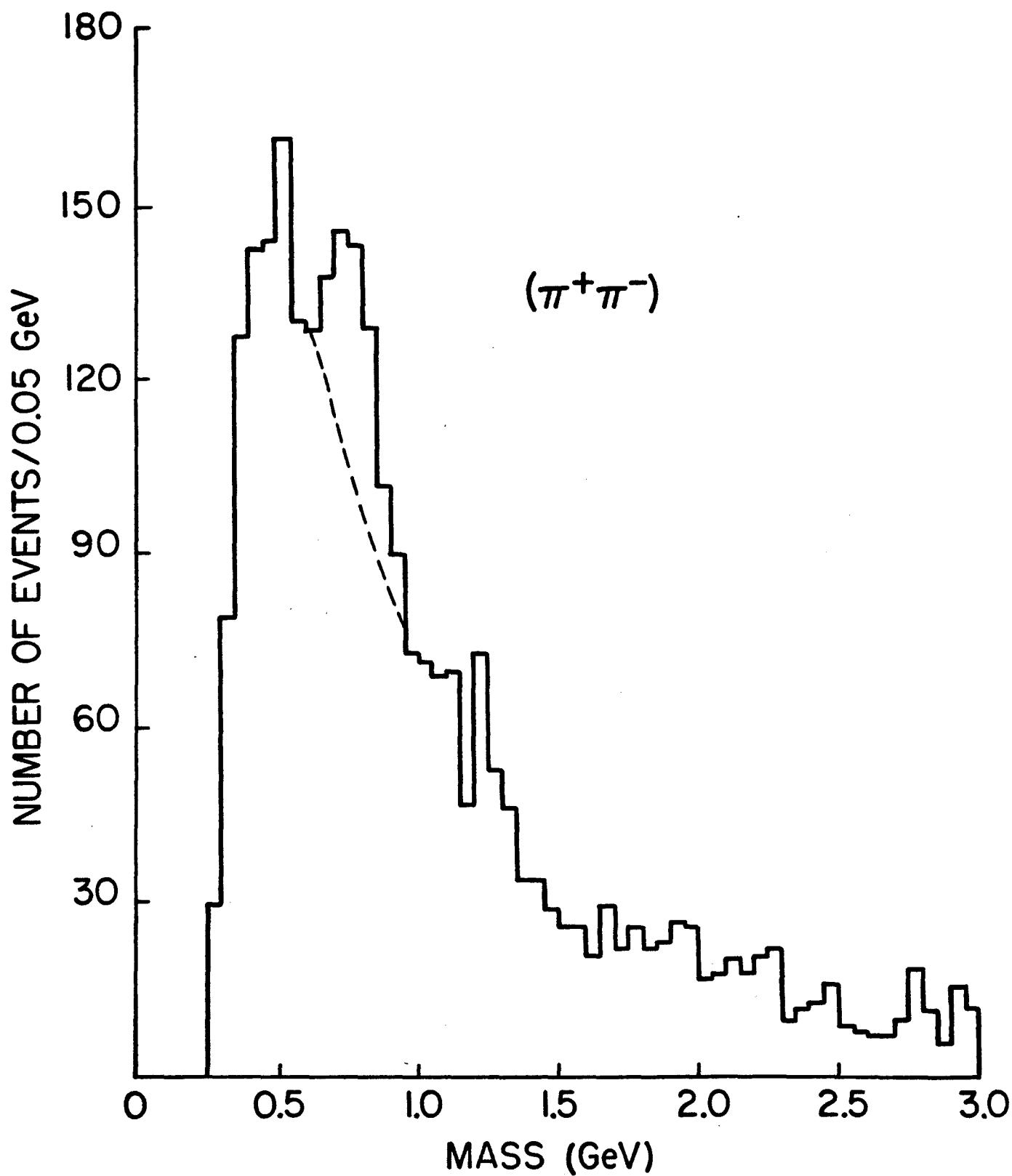Figure V-1: Effective mass distribution for $(\pi^+\pi^-)$ combinations.

TABLE V-1[1,2]

ρ° Production Cross-sections in Four-prong $\pi^- p$ Interactions

P_{lab} (GeV/c)	$\sigma_4 (\pi^- p \to \rho^\circ + X)$ (mb)	
100	.77 ± .16	
147	.9 ± .2	
205	.47 ± .11	
This experiment	250	.42 ± .09 (lower bound; see text)
360	.25 ± .05	

B. $p\pi^{\pm}$

The effective mass distributions for $(p\pi^{+})$ and $(p\pi^{-})$ are shown in Figures V-2 and V-3, respectively. Δ° (1.232 GeV) production is not evident in the $(p\pi^{-})$ distribution, while a Δ^{++} signal is clearly seen in the $(p\pi^{+})$ distribution. There is also a weak signal in the $(p\pi^{+})$ distribution near 2.55 GeV but no corresponding signal in the $(p\pi^{-})$ distribution.

Figures V-2 and V-3 use only identified protons. Since only low-momentum protons are identifiable and this is an error-prone process, a substantial number of protons may be unidentified. Therefore for events with no identified protons both positive tracks have been used as protons in the $(p\pi^{+})$ and $(p\pi^{-})$ effective mass distributions shown in Figures V-4 and V-5, respectively.

In Figure V-4, the Δ^{++} signal is much more pronounced. Using the hand-drawn background, it comprises 183 ± 26 events, corresponding to a cross-section of $.49 \pm .07$ mb. See Appendix C for details of this calculation. Again, this represents a lower bound on the cross-section due to the unknown number of Δ^{++}'s with an LSN3 track. The signal near 2.55 GeV has also become more pronounced. However there is no known resonance in this region, the closest candidate being $\Delta(2420)$.

In Figure V-5 there are peaks near the Λ°(1.115 GeV), the K°_{s} (1.21 GeV, with the π^{+} taken as a proton) and/or the Δ°(1.232GeV), and the ρ° (1.39 GeV, with the π^{+} taken as a proton). In addition a signal exists near 1.9 GeV. The fact that a signal in this region does not also occur in Figure V-3, suggests that this may actually be a $(\pi^{+}\pi^{-})$ resonance. The center-of-mass momentum of the decay products must be near .7 GeV in order for the resonance to be seen near 1.9 GeV in the $(p\pi^{-})$ effective

Figure V-2: Effective mass distributions for (pπ⁺) combinations using only identified protons.
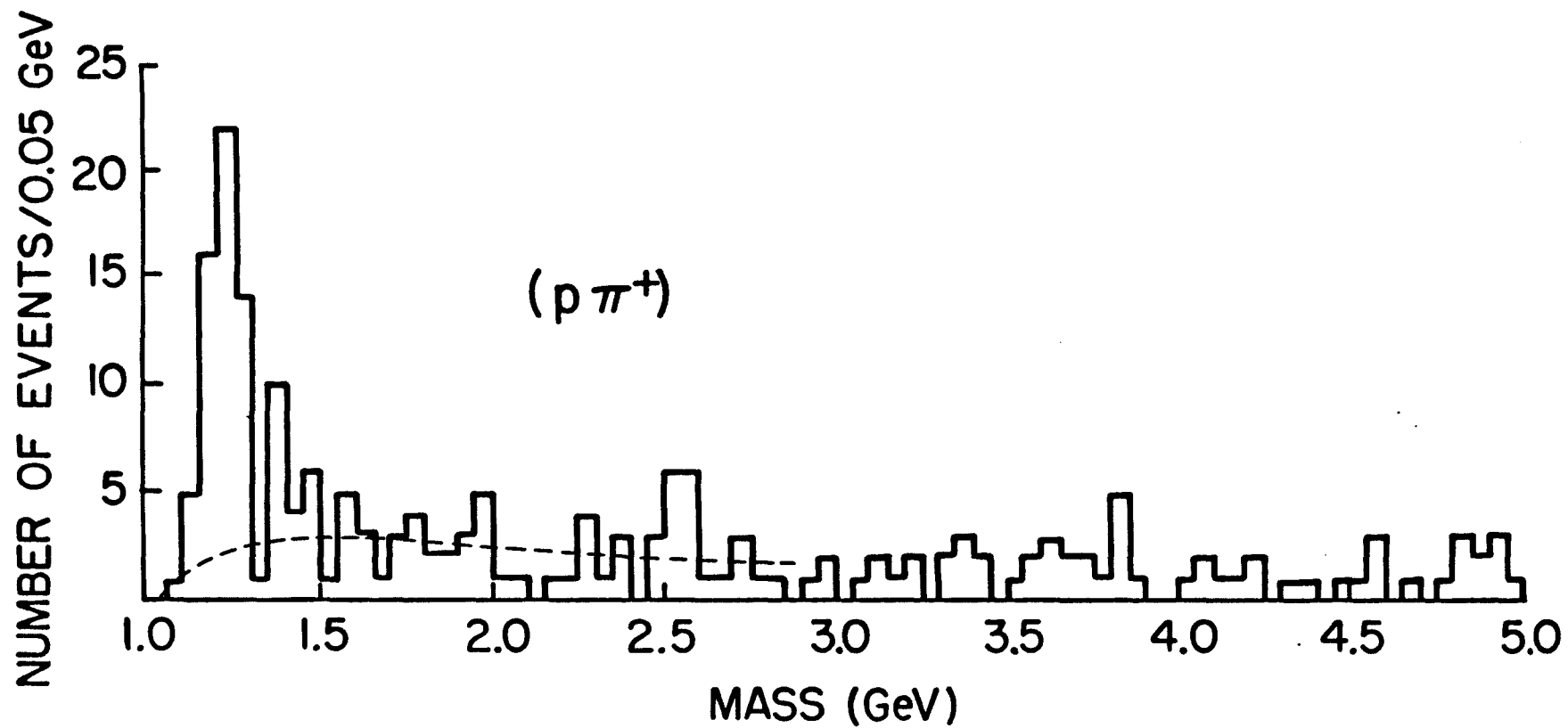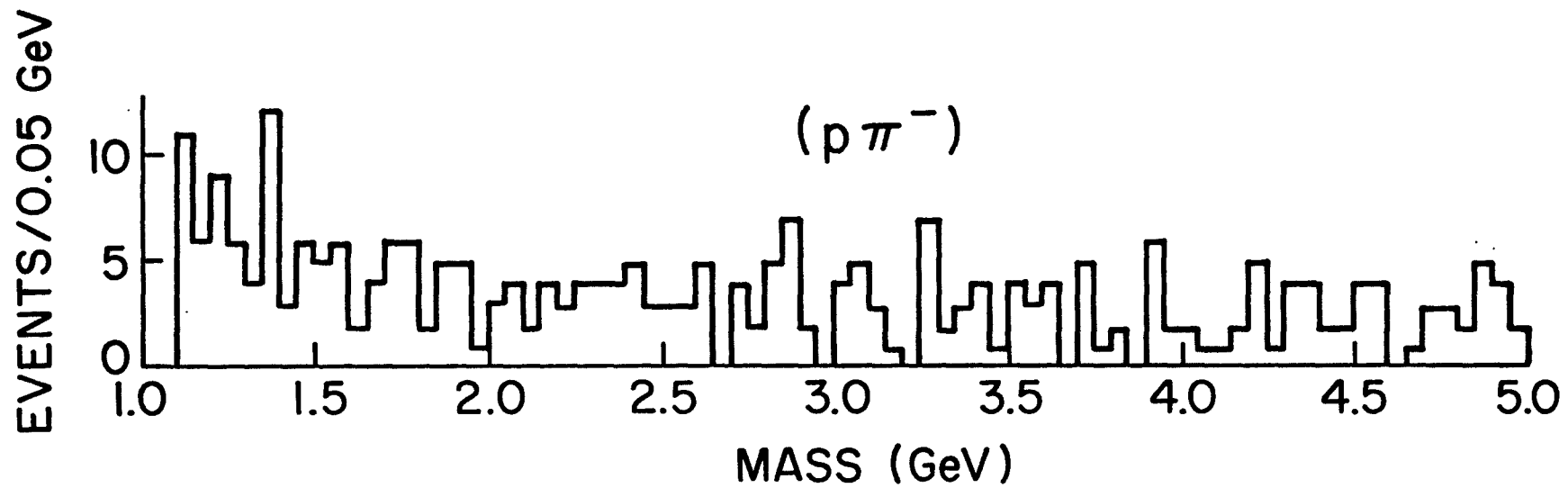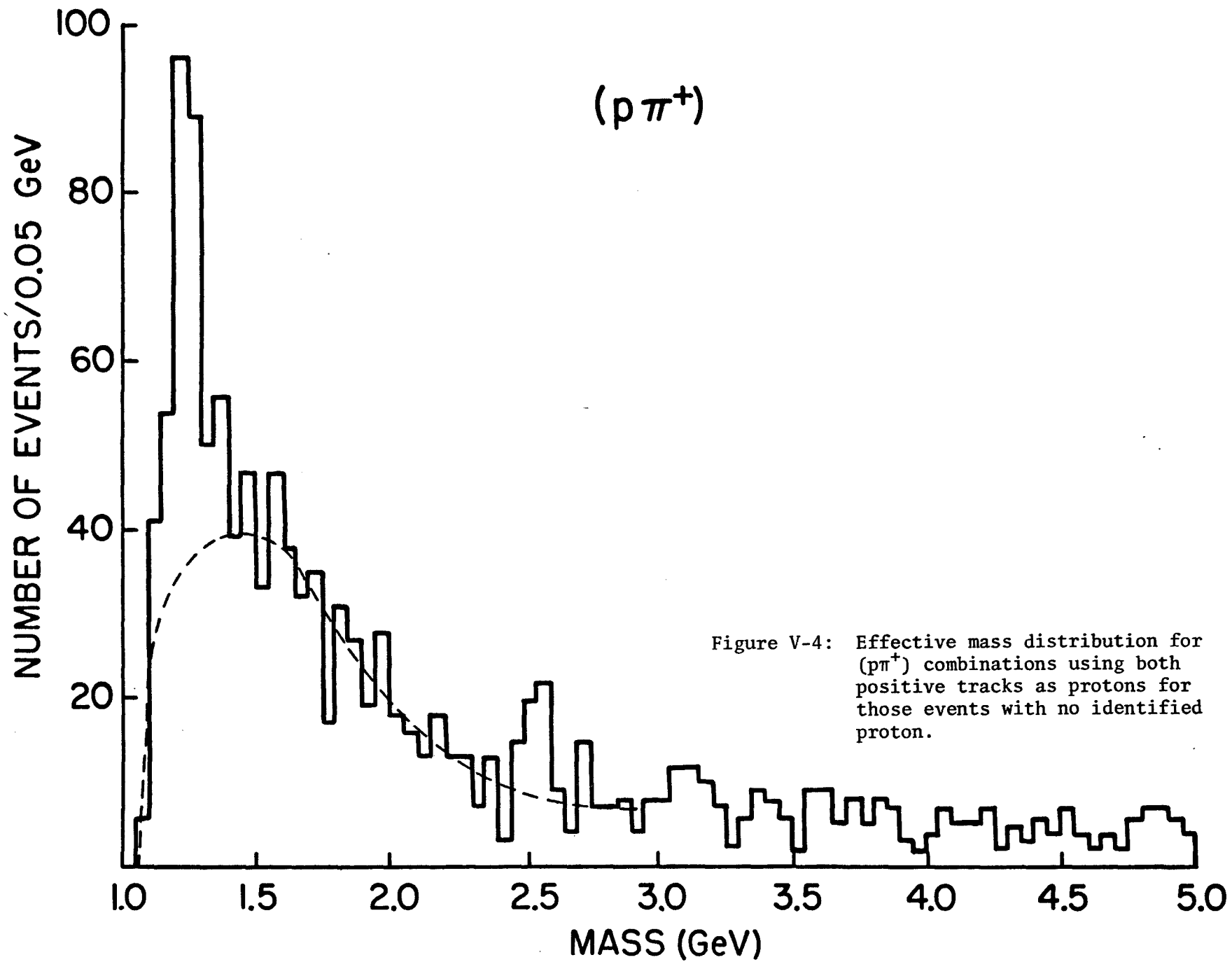
Figure V-3: Effective mass distribution for (pπ⁻) combinations using only identified protons.
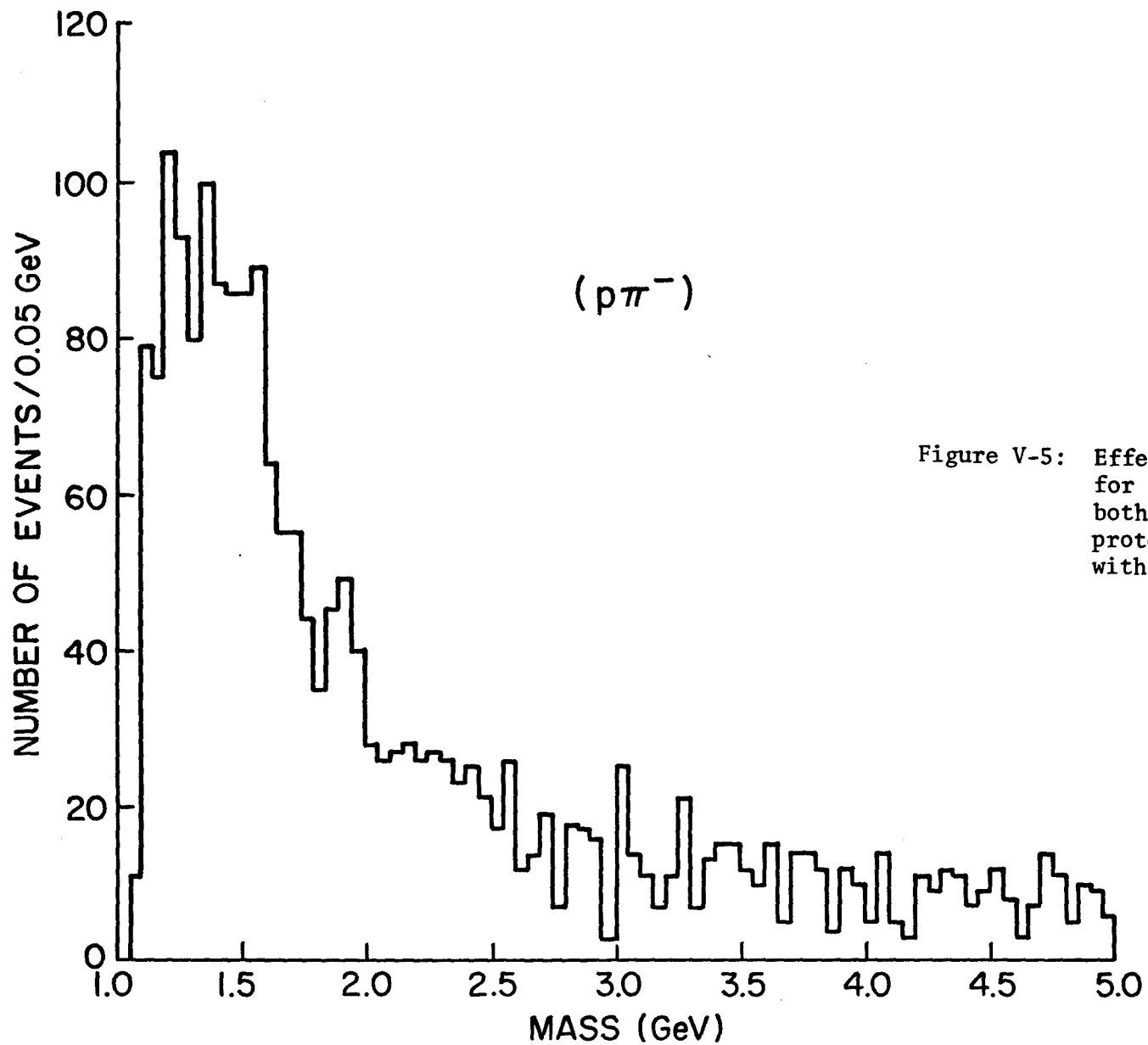
Figure V-4: Effective mass distribution for $(p\pi^+)$ combinations using both positive tracks as protons for those events with no identified proton.

64

Figure V-5: Effective mass distribution for (pπ⁻) combinations using both positive tracks as protons for those events with no identified proton.

mass distribution. However there should be (but there is not) a corresponding peak in the ($\pi^+\pi^-$) effective mass distribution (Figure V-1) near 1.4 GeV. The peak may be due to the presence of the $\Delta(1890)$, $\Delta(1910)$, and/or $\Delta(1950)$.

C. $\pi^+\pi^-\pi^\pm$

The effective mass distributions for ($\pi^+\pi^-\pi^+$) and ($\pi^+\pi^-\pi^-$) combinations are shown in Figures V-6 and V-7, respectively. Both distributions exhibit many peaks which are suggestive of resonance activity but may reflect only the low statistics of the sample. Since the A_1 (mass $\simeq$ 1.1 GeV, width $\simeq$ .3 GeV) and the A_2 (mass = 1.3 GeV, width = .1 GeV) decay via ($\rho\pi$) with branching ratio of 100% and 71%, respectively, a cut was made requiring that one of the ($\pi^+\pi^-$) combinations have an effective mass in the ρ° region (.67 - .87 GeV). The resultant effective mass distributions are shown in Figures V-8 and V-9, respectively. Broad enhancements remain in both distributions, but neither the A_1 nor the A_2 is clearly seen. The signal near 1.8 GeV in Figure V-9 does not correspond to any known resonance.

D. $p\pi^-\pi^\pm$

The effective mass distributions for ($p\pi^-\pi^+$) and ($p\pi^-\pi^-$) combinations are shown in Figures VI-10 and VI-11, respectively. No resonance is evident from either distribution. Using both positive tracks as protons for those events with no identified proton also failed to provide evidence of resonance productions (Figures VI-12 and VI-13).
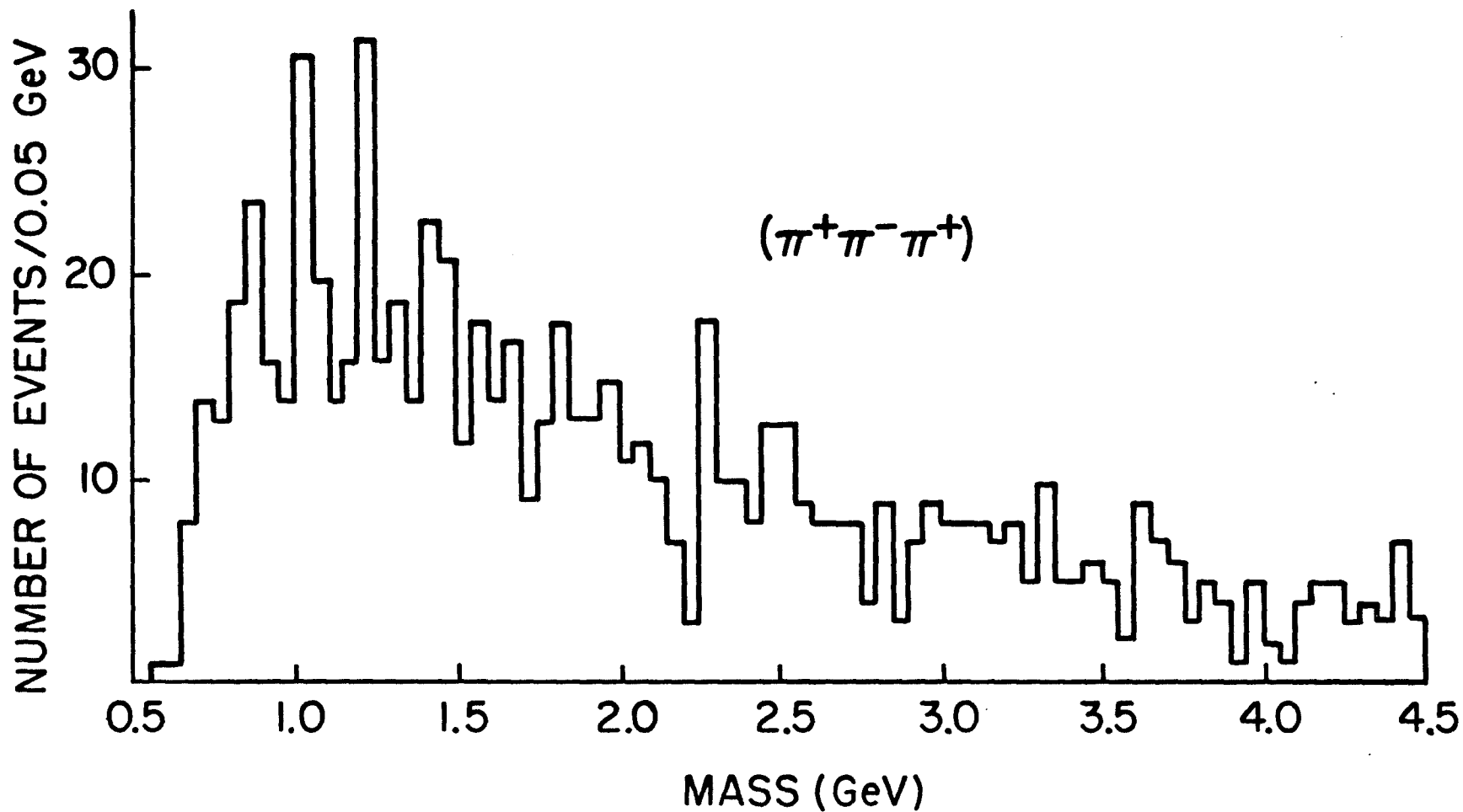
Figure V-6: Effective mass distribution for $(\pi^+\pi^-\pi^+)$ combinations.
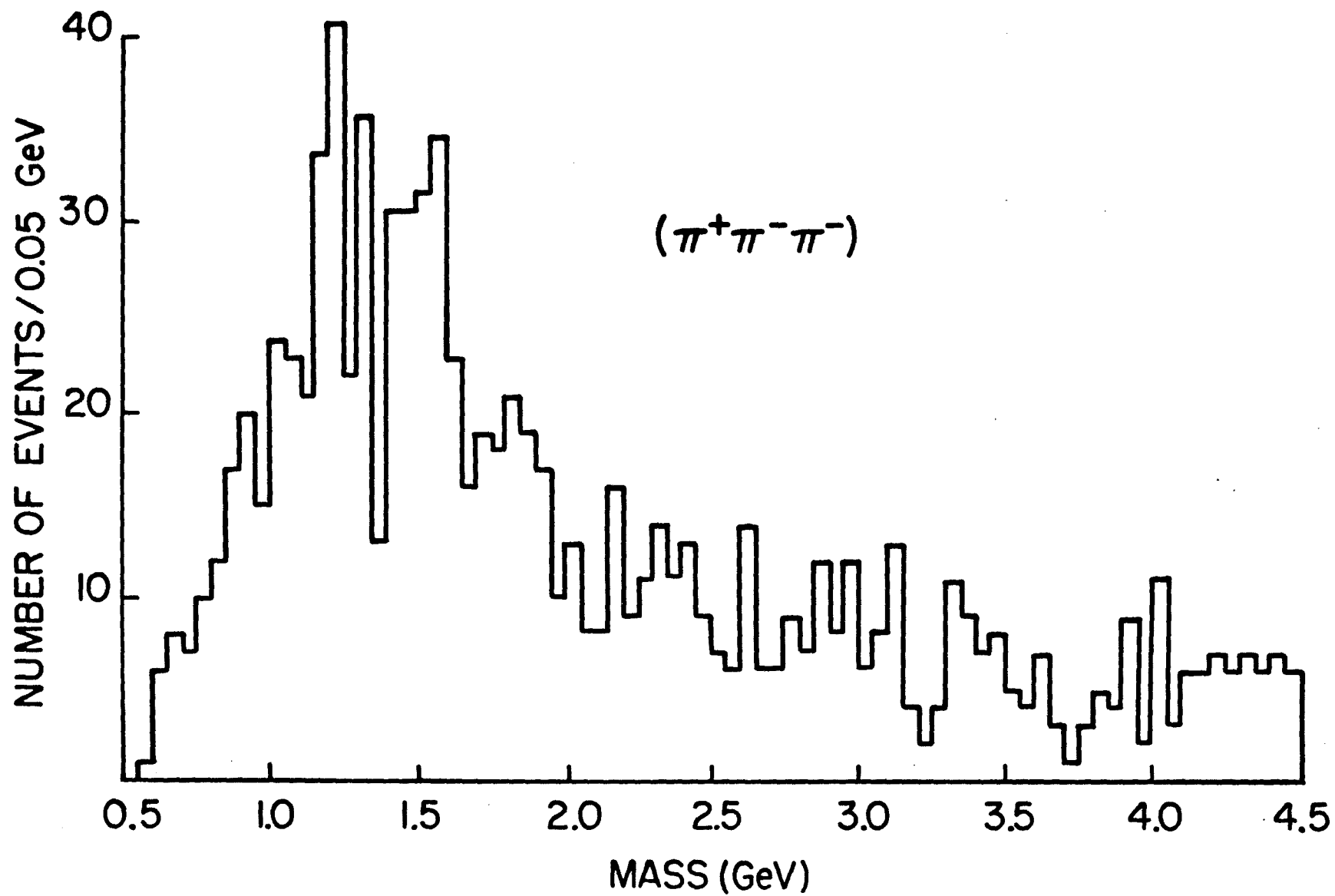
Figure V-7: Effective mass distributions for $(\pi^+\pi^-\pi^-)$ combinations.
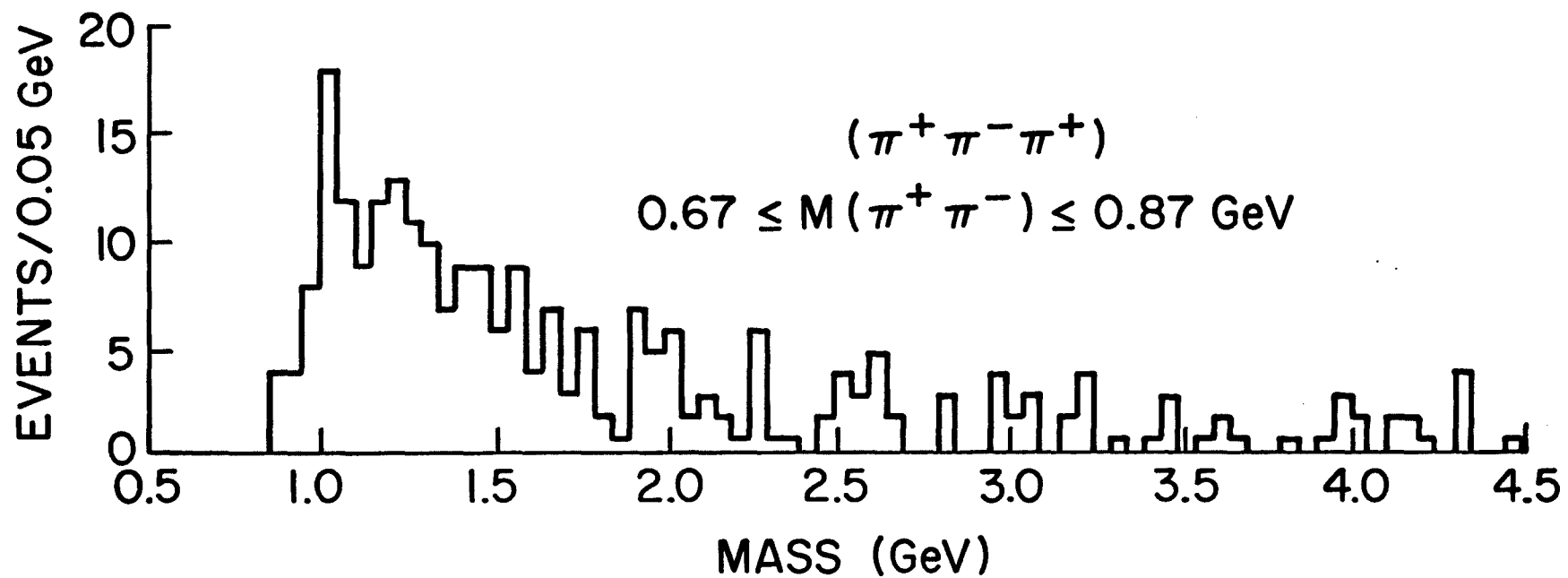
Figure V-8: Effective mass distribution for those $(\pi^+\pi^-\pi^+)$ combinations which have an effective mass of at least one of the $(\pi^+\pi^-)$ combinations in the ρ° region (.67 - .87 GeV).
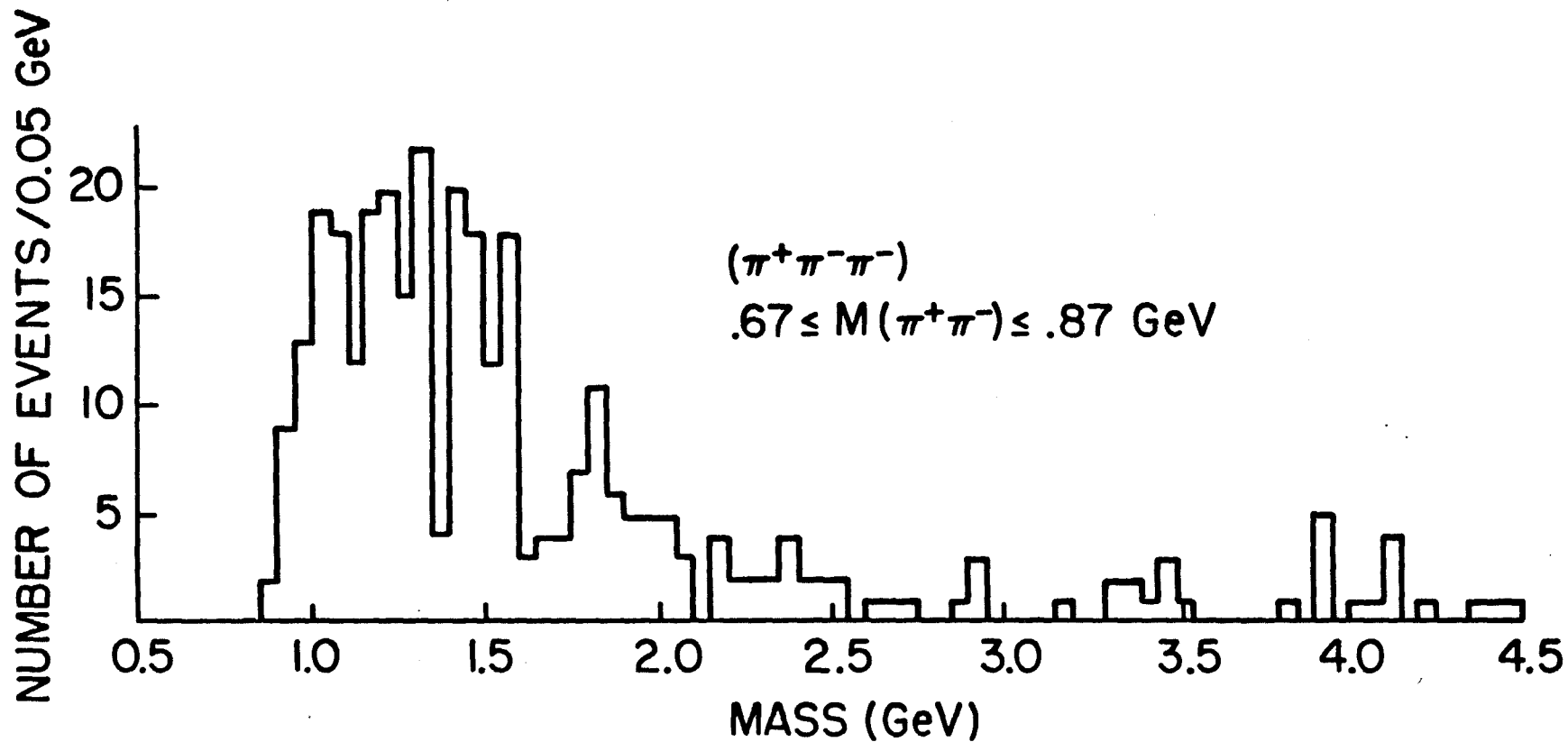
Figure V-9: Effective mass distribution for those $(\pi^+\pi^-\pi^-)$ combinations which have an effective mass of at least one of the $(\pi^+\pi^-)$ combinations in the ρ° region (.67 - .87 GeV).
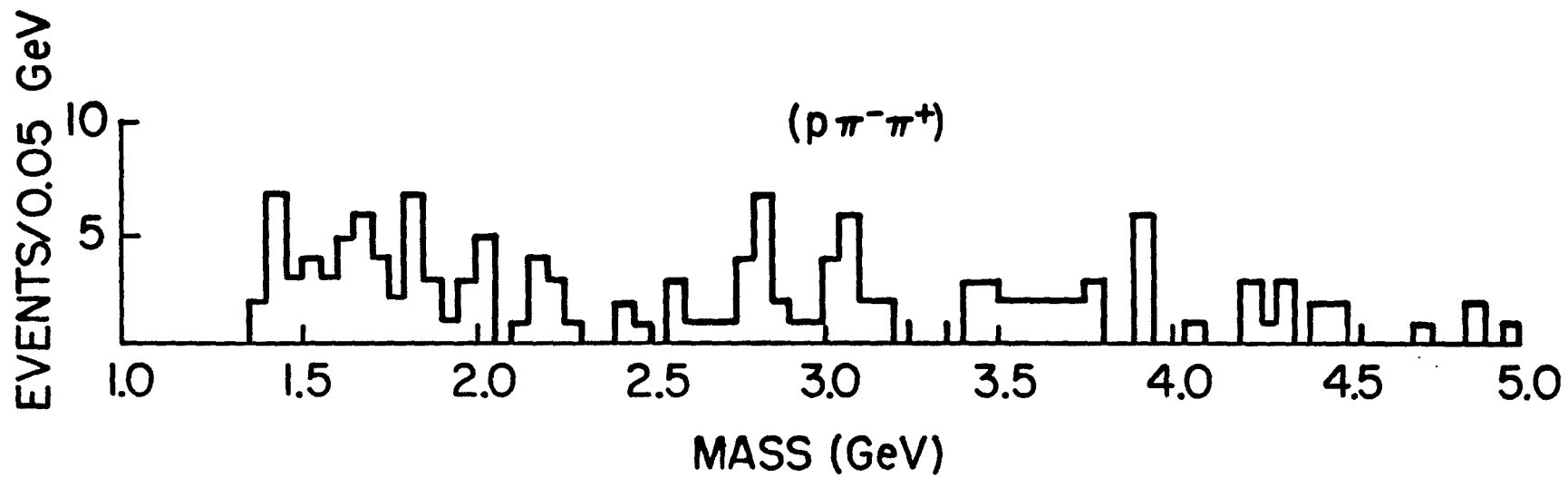
Figure V-10: Effective mass distribution for $(p\pi^-\pi^+)$ combinations using only identified protons.
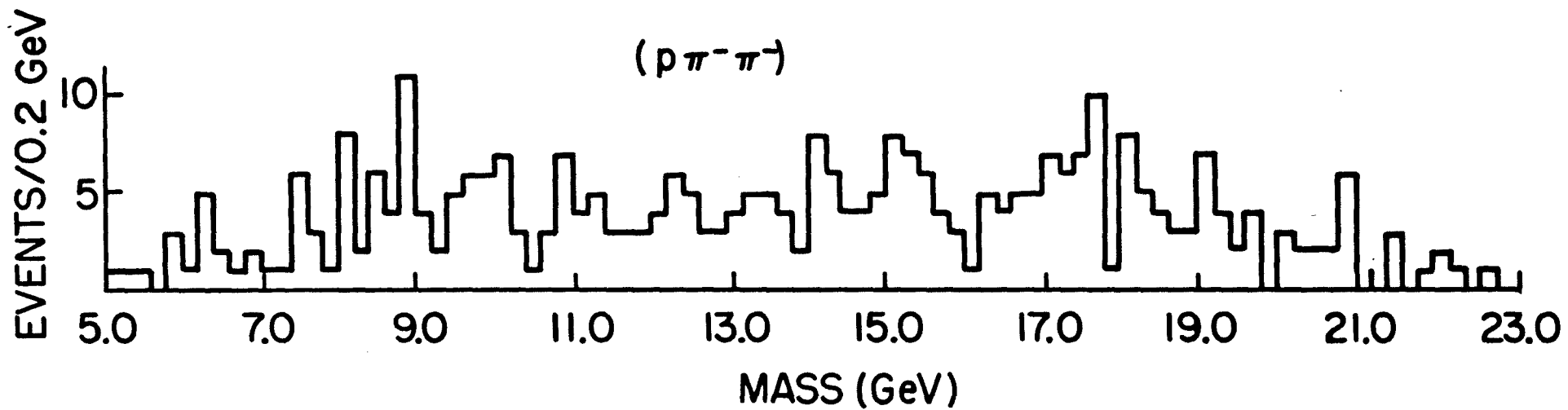
Figure V-11: Effective mass distribution for (pπ⁻π⁻) combinations using only identified protons.

Figure V-12: Effective mass distributions for $(p\pi^-\pi^+)$ combinations using both positive tracks as protons for those events with no identified proton.
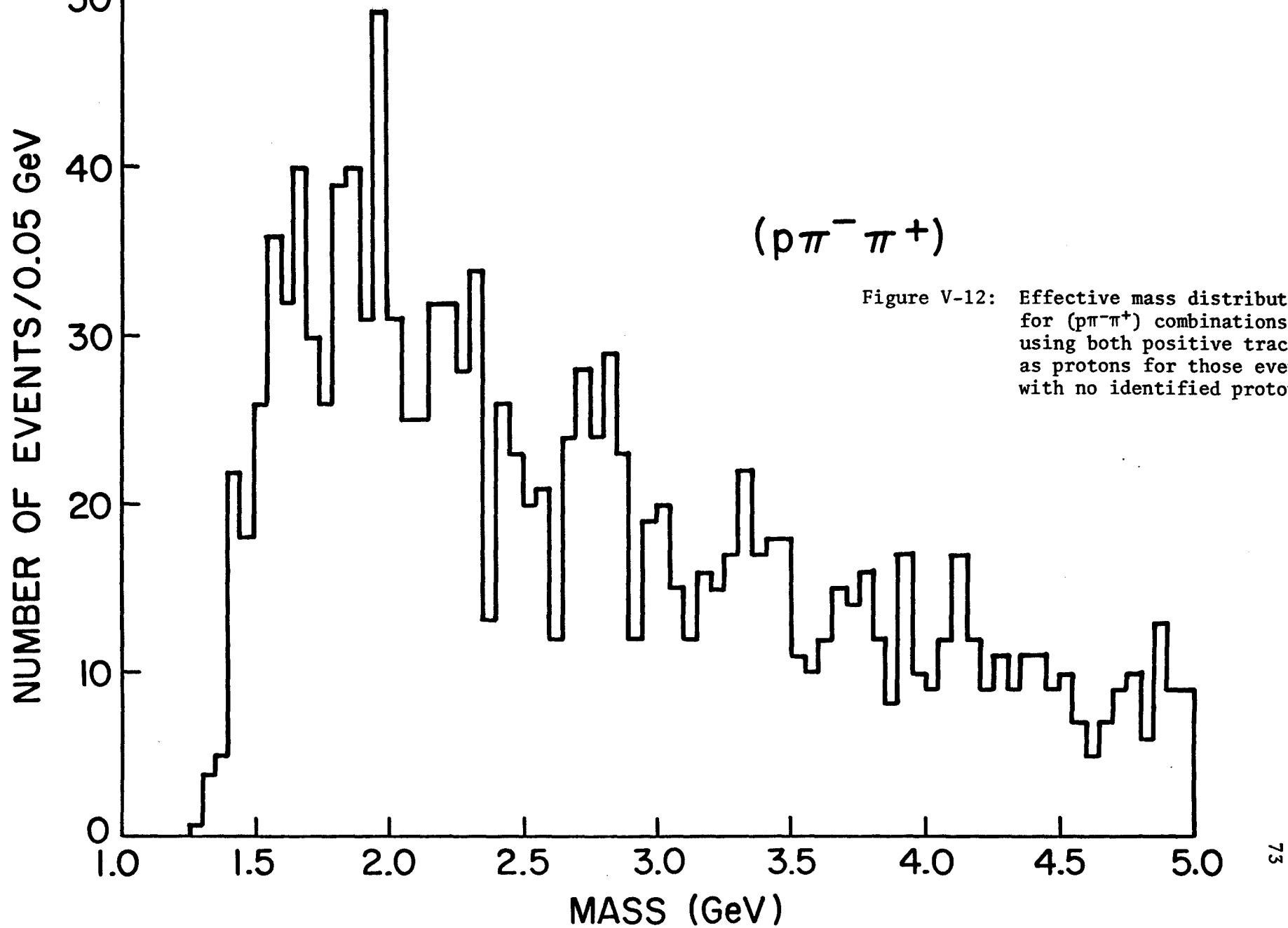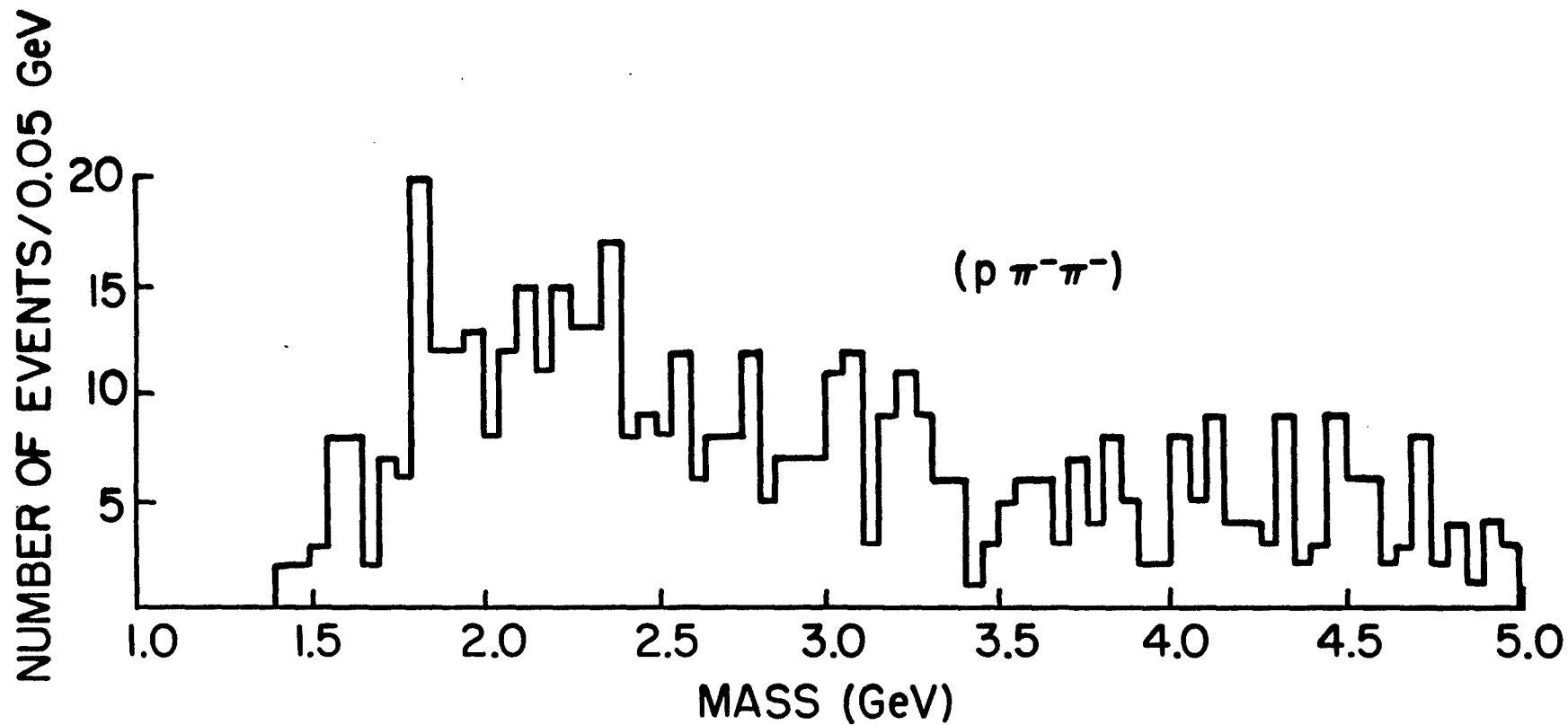
Figure V-13: Effective mass distribution for (pπ⁻π⁻) combinations using both positive tracks as protons for those events with no identified proton.

CHAPTER V.

References

1. P.D. Higgins et al, Phys. Rev. $\underline{D19}$, 65 (1979).

2. F.C. Winkelman et al., Phys. Lett. $\underline{56B}$, 101 (1975).

CHAPTER VI

CROSS-SECTION OF AND RESONANCE PRODUCTION IN THE EXCLUSIVE

REACTION $\pi^- p \to \pi^- \pi^+ \pi^- p$

In this chapter the exclusive reaction

$$\pi^- p \to \pi^- \pi^+ \pi^- p$$

is examined. First the cross-section is determined and the beam and target diffractive components identified. Then results of a resonance search, similar to that of Chapter V , are presented using effective mass distributions of $(\pi^+\pi^-)$, $(p\pi^\pm)$, $(\pi^+\pi^-\pi^-)$, and $(p\pi^-\pi^\pm)$ combinations.

As mentioned in chapter III, all four-prong events successfully passing geometric reconstruction have been fitted to the hypotheses

$$\pi^- p \to \pi^- \pi^+ \pi^- p$$
$$\pi^- p \to \pi^- \pi^+ \pi^- p_{stopping} \ .$$

For three-prong events an impulse proton ($P_x = P_y = 0 \pm 40$ MeV/c, $P_z = 0 \pm 50$ MeV/c) was used in the fit. Any fits not consistent with a measurer-identified proton were rejected. Events with multiple fits had each fit weighted (in addition to the weighting discussed in chapter III) by the inverse of the total number of fits in the event.

A. Cross-Section

Of the 1293.5 events in the data sample, 309.75 were found to have successful fits (using a probability limit in SQUAW of .0001). The resultant chi-squared probability distribution is shown in Figure VI-1. A probability cut, $p > 1.0\%$, has been imposed to reduce background, leaving 242.5 events with fits. Of these

146.5 had 4 constraints,

76.75 had 3 constraints,

19.25 had 1 constraint.

For convenience, hereinafter all events with successful fits will be referred to as 4C events, regardless of the true number of constraints involved.

The 4C cross-section is $625 \pm 80\mu b$, where corrections have been made for the chi-squared probability cut, biases in the data sample, and the scanning efficiencies. See Appendix D for details of this calculation. This value is in good agreement with previously reported values of 670 ± 41 µb at 147 GeV/c[1] and 635 ± 61 µb at 205 GeV/c.[2]

The diffractive nature of the reaction can be seen in Figure VI-2, in which the effective mass of the $(\pi^-\pi^+\pi^-)$ combination is plotted against the smaller of the effective masses of the two $(p\pi^-\pi^+)$ combinations. The majority of events fall into bands with either small $(\pi^-\pi^+\pi^-)$ effective mass or small $(p\pi^-\pi^+)$ effective mass, which are consistent with being the beam and target dissociation regions, respectively. Counting events for which $M(p\pi^-\pi^+) < 5.0$ GeV as target dissociation events and events for which $M(\pi^-\pi^+\pi^-) < 4.0$ GeV as beam dissociation events (and excluding the few events common to both regions), the ratio, R, of beam target dissociation is found to be

$$R = 1.9 \pm .3$$
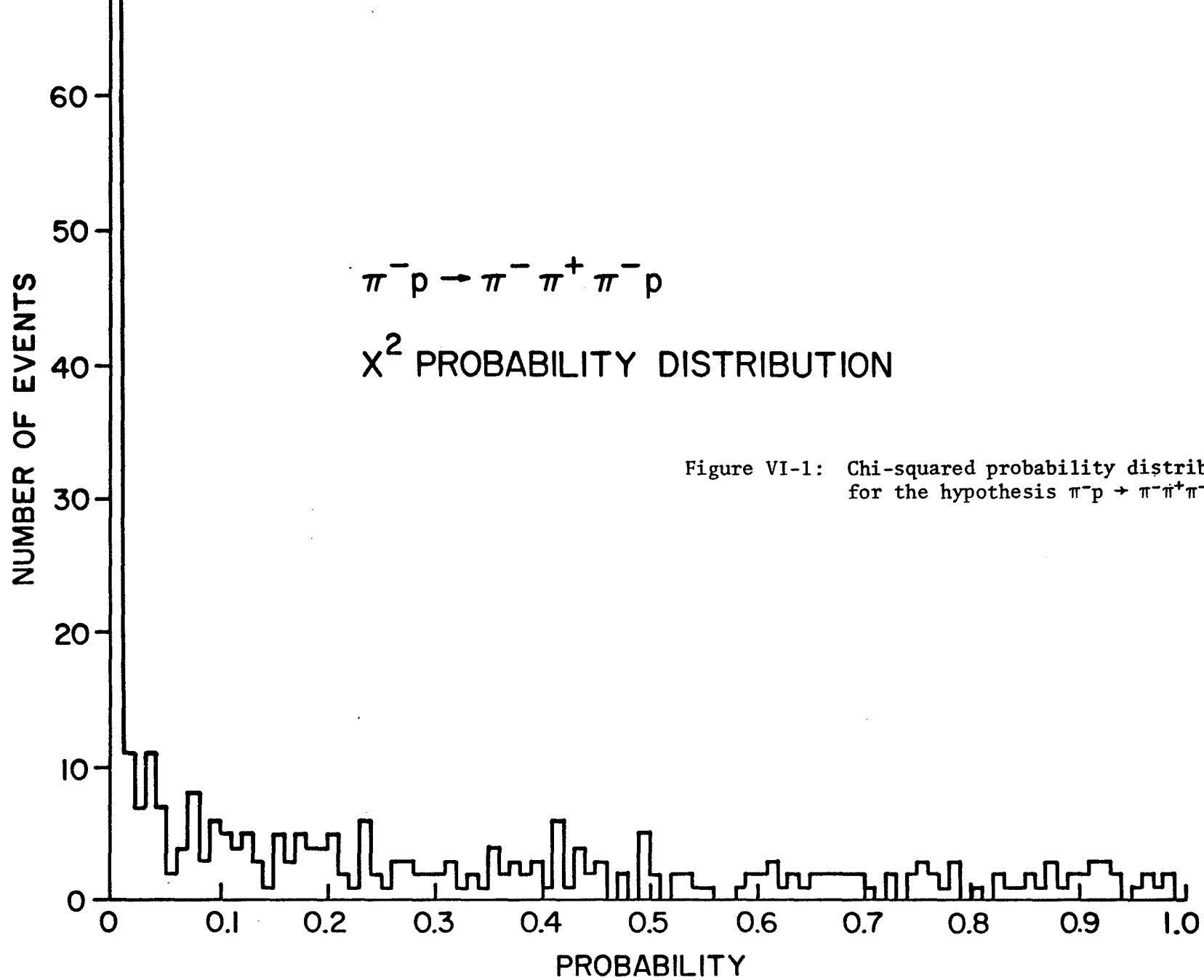
Figure VI-1: Chi-squared probability distribution for the hypothesis $\pi^-p \to \pi^-\pi^+\pi^-p$.
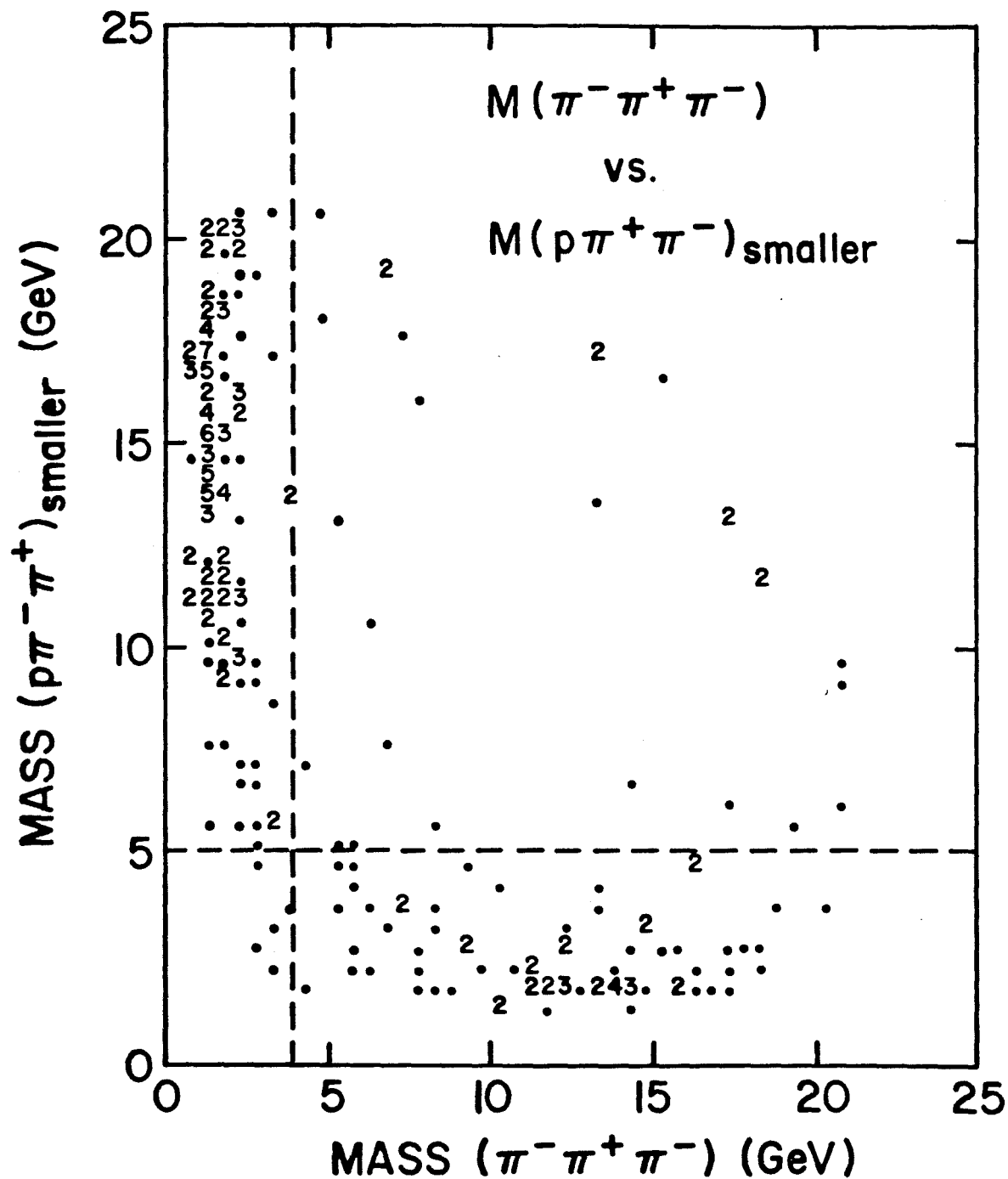
Figure VI-2: Diplot of effective mass of ($\pi^-\pi^+\pi^-$) combinations versus the smaller of the effective masses of the two ($p\pi^-\pi^+$) combinations in the reaction $\pi^-p \to \pi^-\pi^+\pi^-p$.

Events in neither of these bands are non-diffractive in nature. For example they may be due to a single-pion-exchange process, or a low-mass $(\pi^+\pi^-)$ pair may be created in the beam-target center of mass system.

B. $(\pi^+\pi^-)$

The effective mass distribution for $(\pi^+\pi^-)$ combinations is shown in Figure VI-3. There is a very predominant signal in the ρ°(.770 GeV) region. Using the hand-drawn background, there are 58 ± 15 events in the ρ° peak (.6 - .9 GeV), which represent $24 \pm 6\%$ of the 4C sample and correspond to a cross-section of 149 ± 43 µb.

The smoothly decreasing tail extending from .9 GeV to 3.0 GeV shows little evidence of resonance activity, with the exception of a weak signal in the 1.2 - 1.4 GeV region. This may be due to the presence of the f(mass = 1.271 GeV, width = .180 GeV), although low statistics make a more definitive claim difficult.

C. $p\pi^\pm$

The effective mass distributions for $(p\pi^+)$ and $(p\pi^-)$ combinations are shown in Figures VI-4 and VI-5, respectively. The $(p\pi^+)$ distribution has an asymmetrical low-mass peak in the Δ^{++} (1.232 GeV) region. However, due to low statistics and difficulty in determining the background, no attempt has been made to estimate a cross-section for Δ^{++} production. The $(p\pi^+)$ distribution, essentially flat between 1.5 and 5.0 GeV, shows little evidence of any higher-mass resonances.

The broad low-mass peak extending to approximately 1.7 GeV in the $(p\pi^-)$ distribution indicates little, if any, Δ° (1.232 GeV) production. In addition there is little evidence of any higher mass resonances through 5.0 GeV.

Figure VI-3: Effective mass distribution for $(\pi^+\pi^-)$ combinations in the reaction $\pi^- p \rightarrow \pi^- \pi^+ \pi^- p$.

Figure VI-4: Effective mass distribution for $(p\pi^+)$ combinations in the reaction $\pi^- p \rightarrow \pi^- \pi^+ \pi^- p$.

Figure VI-5: Effective mass distribution for ($p\pi^-$) combinations in the reaction $\pi^- p \rightarrow \pi^- \pi^+ \pi^- p$.

D. $\pi^+\pi^-\pi^-$

The effective mass distribution for $(\pi^+\pi^-\pi^-)$ combinations is shown in Figure VI-6. There is a broad peak with a maximum in the 1.2 - 1.3 GeV region and a long tail extending to approximately 2.5 GeV. There is no clear evidence for the existence of either the A_1 (mass $\approx$ 1.1 GeV, width $\approx$ .3 GeV) or the A_2 (mass = 1.312 GeV, width = .102 GeV), or any higher-mass resonances in this distribution. A cut requiring that one of the $(\pi^+\pi^-)$ combinations have an effective mass in the ρ° region (.67 - .87 GeV) has also failed to point out the A_1 or the A_2.

E. $p\pi^-\pi^\pm$

The effective mass distributions for $(p\pi^-\pi^+)$ and $(p\pi^-\pi^-)$ combinations are shown in Figures VI-7 and VI-8, respectively. The low-mass peak in the $(p\pi^-\pi^+)$ distribution has been attributed to the target diffraction component of the interaction (chapter 6, section B). Distributions with bins as narrow as .04 GeV have failed to indicate the presence of resonance activity in this peak.

Both distributions show large accumulations of events at high mass. For target dissociation events each plot contains the fast π^- with slow $(p\pi^+)$ or $(p\pi^-)$, leading to a large effective mass for the combination of three particles. For beam dissociation events the combination of a slow proton with two fast pions also leads to a large effective mass.
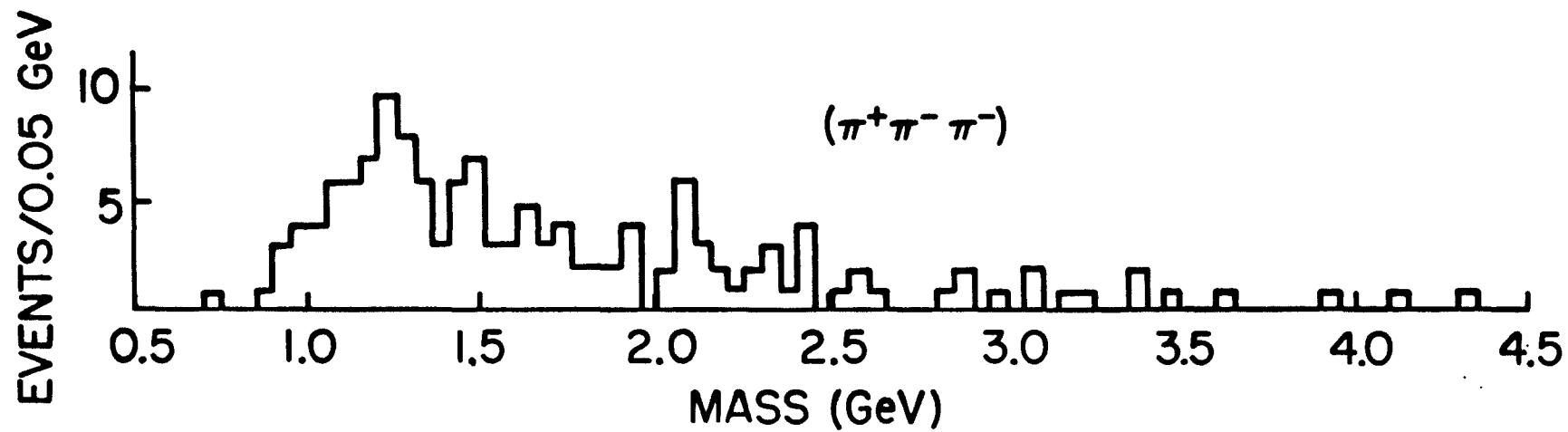
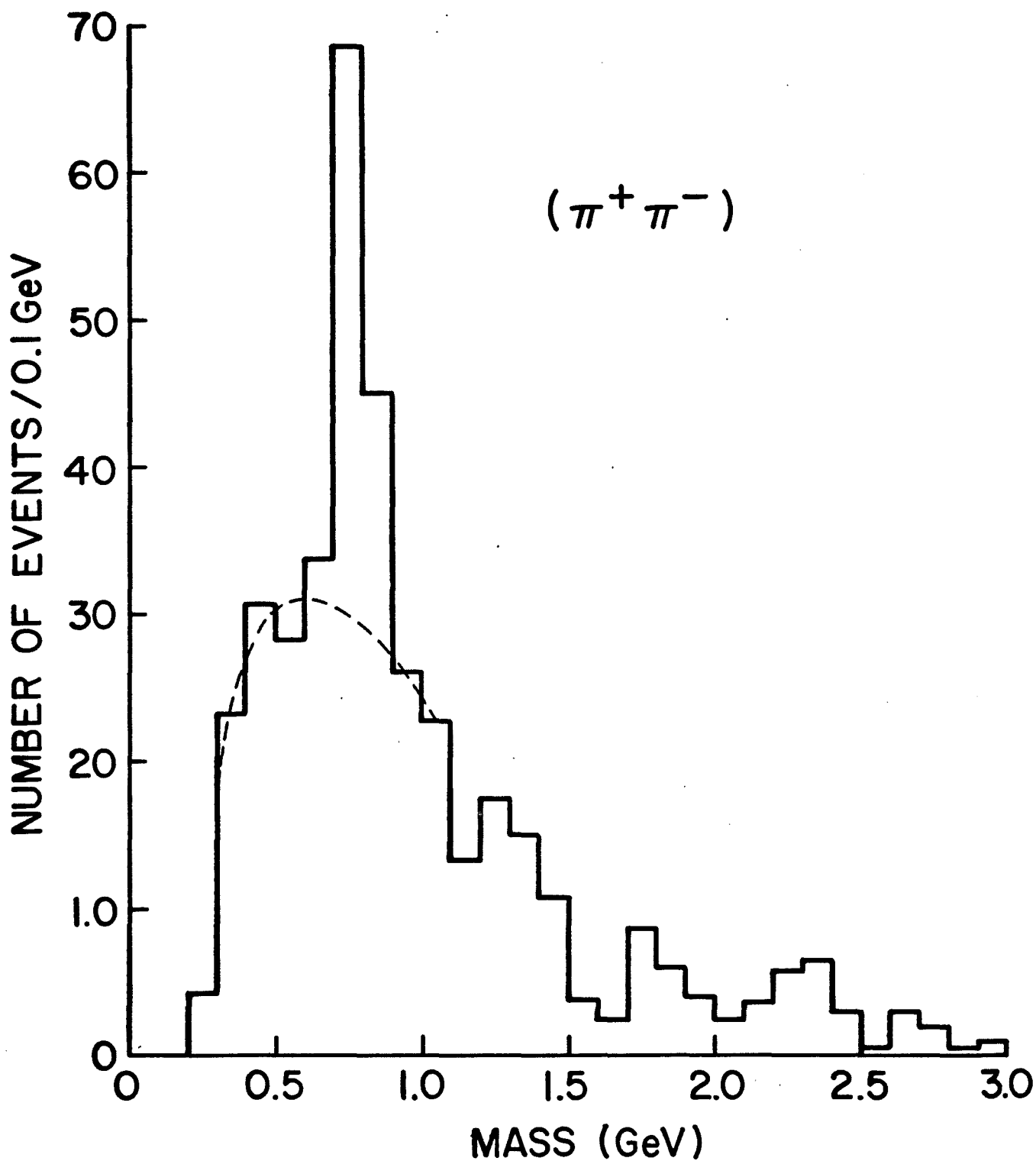Figure VI-6: Effective mass distribution for $(\pi^+\pi^-\pi^-)$ combinations in the reaction $\pi^-p \to \pi^-\pi^+\pi^-p$.
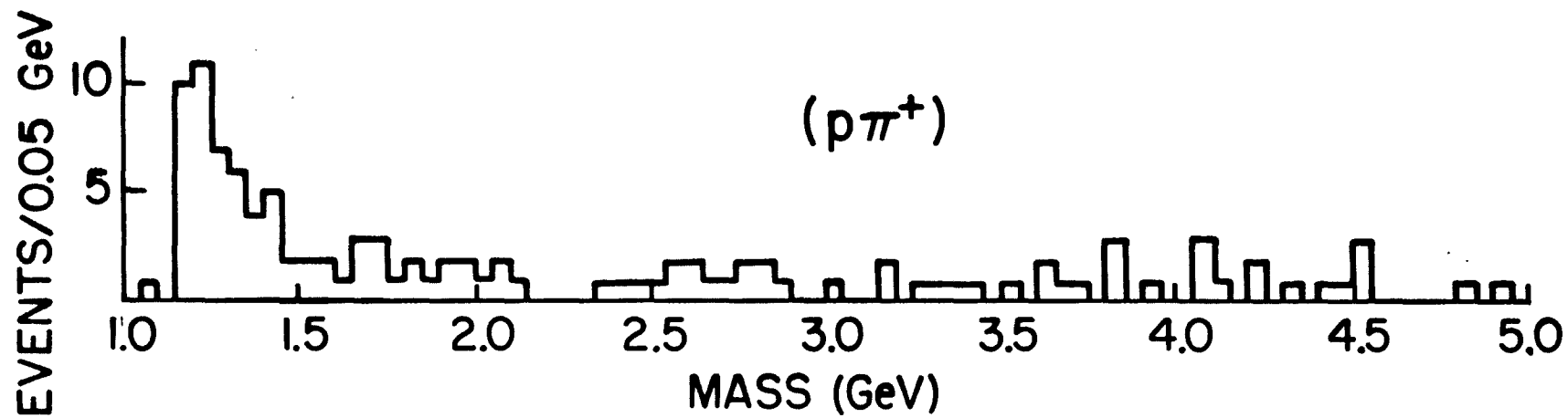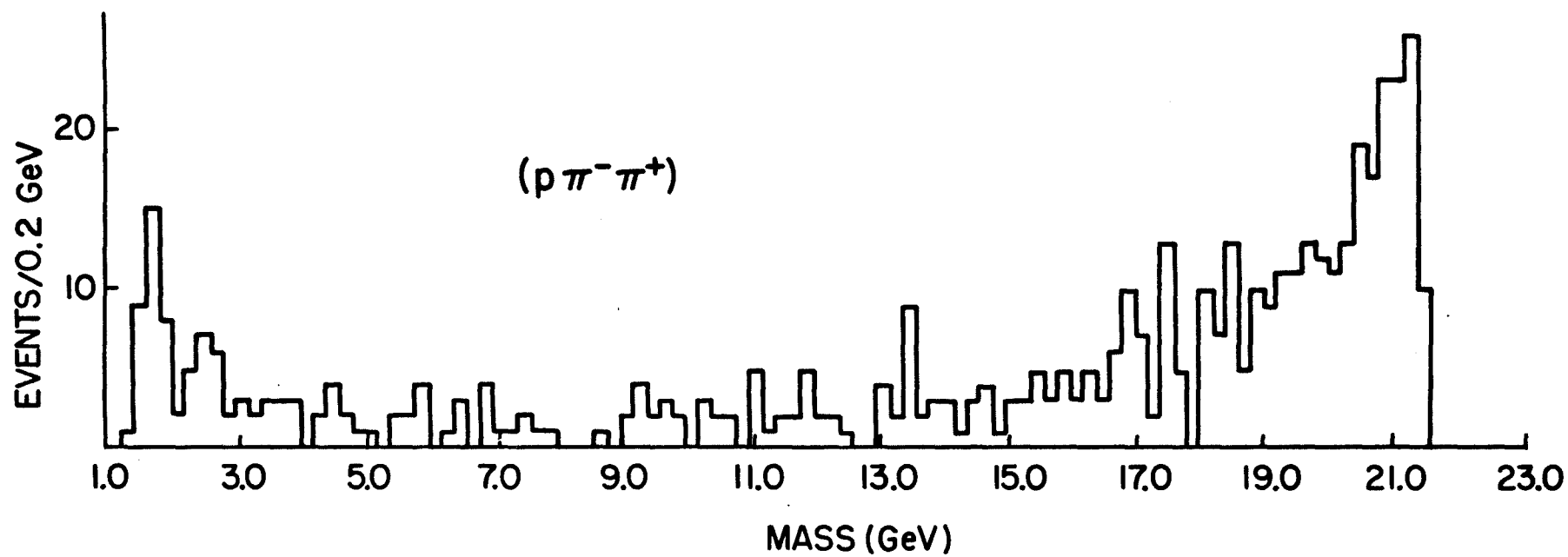
Figure VI-7: Effective mass distribution for $(p\pi^-\pi^+)$ combinations in the reaction $\pi^- p \to \pi^-\pi^+\pi^- p$.

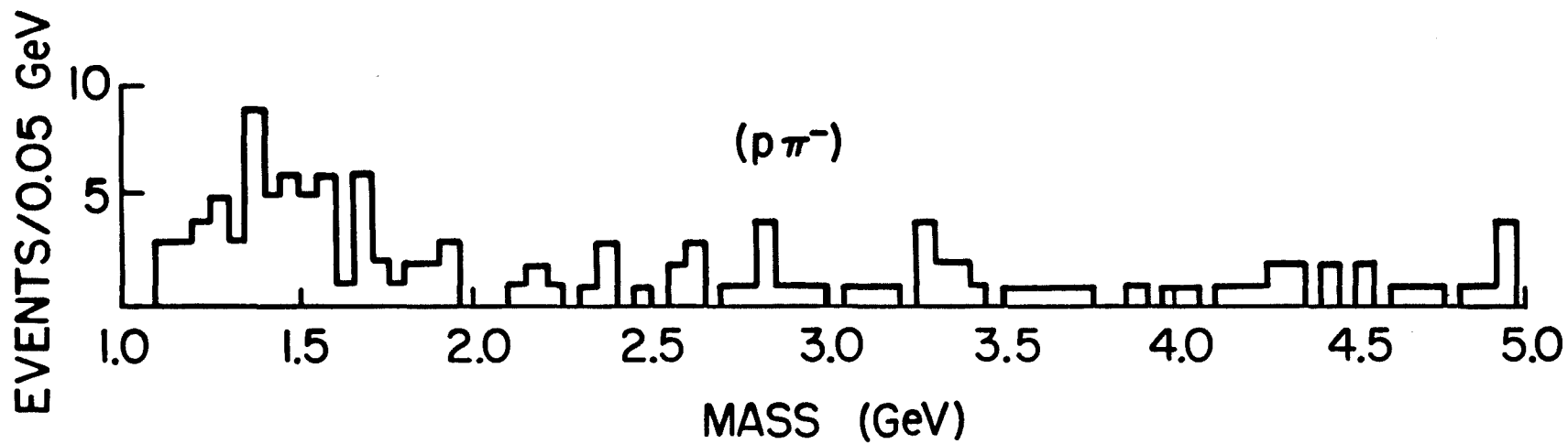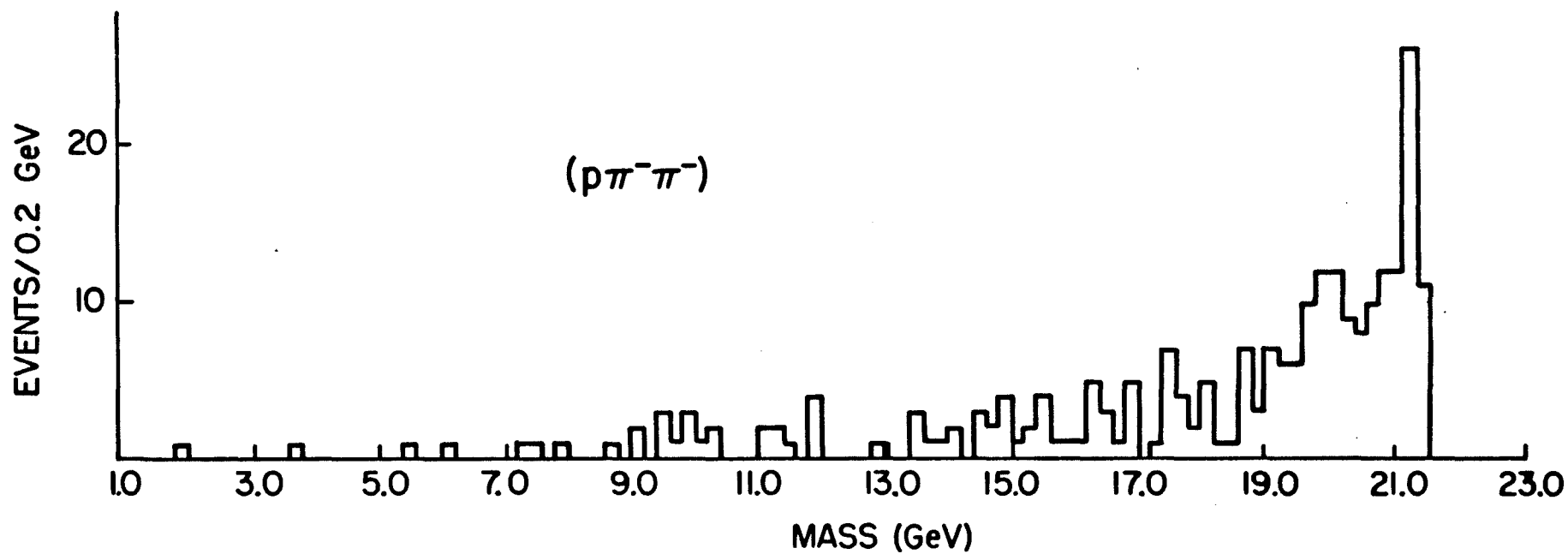Figure VI-8: Effective mass distribution for (pπ⁻π⁻) combinations in the reaction π⁻p → π⁻π⁺π⁻p.

CHAPTER VI

References

1. D. Fong et al., Nuovo Cimento 34A, ser. 2, 639 (1976).

2. H.H. Bingham et al., Phys. Lett. 51B, 397 (1974).

CHAPTER VII

SUMMARY AND CONCLUSIONS

Four-prong $\pi^- p$ interactions at 250 GeV/c were examined with the following goals:

- to study the diffractive nature of the interaction,
- to identify evidence for resonance production and determine inclusive cross-sections when possible,
- to determine the cross-section for the reaction

$$\pi^- p \to \pi^- \pi^+ \pi^- p,$$

  to study its diffractive nature,

  and to study resonance production in this channel.

Analysis of single particle inclusive distributions shows the reaction has significant beam and target diffraction components. The center-of-mass rapidity distributions for inclusive π^- production is dominated by a large peak at positive rapidity. The analogous distribution for inclusive π^+ production exhibits peaks at both positive and negative rapidities. Both distributions are relatively depleted in the central region. More direct evidence of target dissociation is seen in the Feynman X distribution for inclusive π^- production, in which a peak near $X_F = .8$ corresponds to the leading pion. The distribution of the square of the effective mass of the system recoiling from the proton, which exhibits a large low-mass peak, demonstrates beam dissociation at masses up to 6 GeV.

Effective mass distributions of $(\pi^+\pi^-)$, $(p\pi^\pm)$, $(\pi^+\pi^-\pi^\pm)$ and $(p\pi^-\pi^\pm)$ combinations were examined for evidence of resonance production. Substantial $\rho^o(770)$ and $\Delta^{++}(1232)$ production is evident with lower bounds on their respective cross-sections of $.42 \pm .09$ mb and $.49 \pm .07$ mb, respectively. Broad enhancements near the A_1 and A_2 appear in the $(\pi^+\pi^-\pi^\pm)$ distributions, but are not separable from the backgrounds. There is also an enhancement near 1.2 GeV in the $(\pi^+\pi^-)$ distribution which may be due to the presence of f(1271). Weak, unexplained signals exist near 2.5 GeV in the $(p\pi^+)$ distribution and near 1.9 GeV in the $(p\pi^-)$ distributions.

Using a probability cut of .01, 242.5 events successfully fit the hypothesis

$$\pi^- p \rightarrow \pi^-\pi^+\pi^- p.$$

After correcting this number for the probability cut, biases in the data, and the scanning efficiencies, the cross-section is found to be 625 ± 80 μb. The reaction is dominated by beam and target diffractive dissociation in the ratio of $1.9 \pm .3$ to 1. A resonance search was made using all possible two- and three-body effective mass distributions. The only resonance clearly identified is the ρ^o, which has been found to occur in $24 \pm 6\%$ of the events in this channel, corresponding to a cross-section of 149 ± 43 μb.

APPENDIX A: Measurement Tape Format

This appendix describes the format of the raw measurement tape

supplied to the University of Maryland and procedures used to read it.

There are no label records and all data is contained within 1 file.

Each logical record comprises a single physical record on the tape.

The tape cannot be read by an unformatted FORTRAN read statement, so

NTRAN[1] was used. All words on the tape are right adjusted integers

consisting of 40 bits each. Words were compressed to 36 bits (1108

word size) by deleting the first 4 bits (all zeros) of each word. A

new tape was then written using a standard FORTRAN unformatted write

statement.

The first word in each record contains the "count", i.e. the

number of words that follow in the remainder of the record. Following

is the indicative block, the fiducial coordinates block, the track coor-

dinates block, the TAVL table, and the AFTRK table.[2] The contents of

these blocks is described below.

<div align="center">Indicative Block (18 words)</div>

Word Number	Information
1	Number of tracks in each view times 2**18 + the "count"
2	Experiment number
3	Roll number
4	Frame number

Word Number	Information
5	Event topology as measured:

1000 * number of prongs at primary vertex

+ 100 * number of prongs at primary vertex which kink and for which the track after the kink is measured

+ 10 * number of "vees" (gamma conversions and/or strange particle decays)

Word Number	Information
6	Measurement number
7	Measurer ID
8	Date measured (MMDDYY)
9	Measuring table
10	Event topology as scanned
11	Unused
12	Event topology as measured (again)
13	Packed indexing word (unused by geometry program)
14	Zone of third kink or vee
15	Zone of second kink or vee
16	Zone or first kink or vee
17	Zone of primary interaction
18	Reject code. If non-zero, signals end of record.

The Fiducial coordinates block (144 words)

Word Number	Information
1	Fiducial 1, View 1, X coordinate
2	Fiducial 1, View 1, Y coordinate
3	Fiducial 1, View 2, X coordinate
4	Fiducial 1, View 2, Y coordinate

.

Word Number	Information
.	
.	
.	
7	Fiducial 1, View 4, X coordinate
8	Fiducial 1, View 4, Y coordinate
9	Fiducial 2, View 1, X coordinate
10	Fiducial 2, View 1, Y coordinate
.	
.	
.	
143	Fiducial 18, View 4, X coordinate
144	Fiducial 18, View 4, Y coordinate

The track coordinates block (variable length)

The measuring procedure determines the order of tracks within this block. All the tracks are measured in View 1, then all the tracks are measured in View 2, etc. Within each view, first the beam track is measured (backward from the primary vertex), then all tracks eminating from the primary vertex, then each track that follows a kink, then tracks comprising vees. If a vertex is not measured in a view, the coordinates X = 0, Y = 0 appear as the first measured point for each track originating at that vertex.

The TAVL table (4 times number of tracks)

The TAVL table provides the index for the track coordinates block. TAVL entries are of the form: 2^{18} times (number of points for this track in this view) + (location of the track bank relative to the start of the track coordinate block). The entries are in the same order as

in the track coordinates block: track 1, view 1; track 2, view 1;...;
last track view 1; track 1, view 2; track 2, view 2;...;last track view
4.

The AFTRK table (1 times number of tracks)

AFTRK entries are of the form: 10000 * upstream vertex number +
1000 * downstream vertex number + 100 * view 1 track code + 10 * view 2
track code + view 3 track code. The last word in the event record is
the AFTRK entry for the last track measured.

APPENDIX A

References

1. Available in the Fortran V library of supplied functions.

2. Between the track coordinates block and the TAVL table is an additional block of information not used by the geometry program.

APPENDIX B: DST Format

ID Block (75 Words)

Word Number	Information
1	Experiment Number
2	1st 2 Digits of Frame
3	Last 4 Digits of Frame
4	Zone
5	Measurement Number
6	Event Topology as Measured
7	True Event Topology
8	Input Record Number
9	Flag for Shortened Tracks
10	Number of Matches
11	Default Match Flag
12-20	Unused
21	Pointer to First Data Word (=44) For Update
22-32	Match Words
33-43	Track Codes
44	Trigger (B.C. Pickup Command)
45	Unused
46	Machine No.
47	Unused
48	Measurer's ID
49	Unused
50	Date Measured
51	Unused
52	Date Tp'ed
53-55	Unused
56	Date Squawed
57-59	Unused
60	Version Number of Arrow
61	X for Vertex
62	Y for Vertex
63	Z for Vertex
64-72	Unused
73	# of Missing Masses + (100*Address of First One)
74	# of Truncated Fits + (100*Address of First One)
75	# of Full Fit Blocks + (100*Address of First One)

TVGP Track Block (45 Words, one for each TVGP mass interpretation for each track)

Word Number   Information

Word Number	Information
1	TP Track Number
2	Unused
3	Mass (Carries Sign of Charge)
4	LSN * 10 + SPMC
5	L
6	AZ ⎫
7	DIP ⎬ Beginning
8	Momentum ⎭
9	DL
10	X ⎫
11	Y ⎪
12	Z ⎪
13	D-AZ-D-DIP ⎬ Beginning
14	D-AZ-D-MOM ⎪
15	D-DIP-D-MOM ⎭
16	AZ ⎫
17	DIP ⎬ End
18	MOM ⎭
19	D-AZ ⎫
20	D-DIP ⎬ Beginning
21	D-MOM ⎭
22	FRMS
23	Unused
24	CRMS
25	Unused
26	Ionization
27	KPT
28	Failure Code
29	Track Code
30	# of Points/View
31	Match Word
32	Match Word
33	CM Rapidity
34	D (CM Rapidity)
35	Feynman X
36	D (Feynman X)
37	P Parallel
38	P Perpendicular
39	Cos Theta CM WRT Beam
40	Phi About the Beam
41	P Parallel (CM)
42	Velocity (LAB)
43	X ⎫
44	Y ⎬ End
45	Z ⎭

SQUAW Fit Blocks

Truncated Fit Block (6 words each)

Word Number	Information
1	Number of Tracks
2	Unused
3	Reduced Mark Number
4	Probability Word
5	Reject Number
6	Codes for Reason Truncated:

    1 Too Little Room for Fit
    2 Unphysical Because Track Ignored
    3 Unused
    4 SQUAW Reject Report

Full Fit Block (ID Block Followed by Track Blocks)

ID Block (5 words per fit)

Word Number	Information
1	Number of Tracks in Fit
2	Not Used
3	Reduced Mark Number
4	Probability Word
5	Reject Number

Fitted Track Blocks for the Fit (20 Words per Track)

Word Number	Information
1	TP Track Number
2	Flag (Currently SWUM)
3	Mass
4	Azimuth
5	DIP
6	Momentum
7	D-AZ
8	D-DIP
9	D-MOM
10	CM Rapidity
11	D-CM Rapidity
12	Feynman X
13	D-Feynman X
14	P-Parallel
15	P-Perpendicular
16	Cos Theta CM WRT Beam
17	Phi About the Beam
18	Stretch Phi
19	Stretch S
20	Stretch K

APPENDIX C

Details of the Calculations of the Cross-sections for ρ°(770) and Δ^{++}(1232)

Production

The cross-sections for ρ°(770) and Δ^{++}(1232) production are determined

from

$$\sigma_R = \frac{N_R(L_1 \leq mass \leq L_2)}{N_4} \sigma_4$$

where σ_R is the cross-section for the resonance

$N_R(L_1 \leq mass \leq L_2)$ is the number of events in the resonance

signal above background within the mass limits L_1 and L_2

For ρ°, L_1 = .6 GeV

L_2 = .95 GeV

N_R = 156 ± 32

For Δ^{++}, L_1 = 1.05 GeV

L_2 = 1.5 GeV

N_R = 183 ± 26

The error assigned to N_R includes statistical uncertainties in

the peak and in the background.

N_4 is the number of four-prong events in the data sample. Based

on the scanning biases discussed in chapter III, there are

an estimated 1233 ± 5 four-prong events, the rest being two-

prong events with a close-in neutral particle decay or a

dalitz pair.

σ_4 is the four-prong cross-section, 3.32 ± .10 mb.

APPENDIX D

Details of the calculation of the cross-section for the reaction

$$\pi^- p \rightarrow \pi^- \pi^+ \pi^- p.$$

There were 3105 observed three- and four-prong events, of which 1293.5 are represented in the data sample. The cross-section for the reaction

$$\pi^- p \rightarrow \pi^- \pi^+ \pi^- p$$

has been determined from the formula

$$\sigma_{4C} = [(N_1 + N_2 + N_3) \frac{3105}{1293.5} + N_4] \left(\frac{\varepsilon_i}{\varepsilon_f}\right)\left(\frac{1}{M}\right)$$

where

N_1 = 242.5 ± 16 observed 4C events,

N_2 = 10 ± 5 events added to correct for the chi-squared probability cut, $p > .01$,

N_3 = 0 ± 25 events to estimate the uncertainty in the background,

N_4 = 3 ± 1 events estimated to be 4C events in the 14 ± 4 events missing from the observed sample due to unresolved secondary interactions,

ε_i = .943 ± .004, the probability that a four-prong vertex was classified correctly. The primary factor involved is the classification of a secondary interaction as a primary interaction.

ε_f = .919 ± .005, the probability of finding a four-prong vertex.

M = 1.00 ± .02 events/μb, the microbarn equivalent.